Single-Molecule Magnets: Preparation and Properties of Low Symmetry [Mn₄O₃(O₂CPh-R)₄(dbm)₃] Complexes with S = ⁹/₂

Núria Aliaga-Alcalde,† Rachel S. Edwards,‡ Stephen O. Hill,‡
Wolfgang Wernsdorfer,§ Kirsten Folting,‖ and George Christou*,†

*Conttribution from the Departments of Chemistry and Physics, University of Florida,
Gainesville, Florida 32611, Laboratoire Louis Néel-CNRS, BP 166, 25 Avenue des Martyrs,
38042, Grenoble, Cedex 9, France, and Department of Chemistry and Molecular Structure
Center, Indiana University, Bloomington, Indiana 47405-7102*

Received May 6, 2004; E-mail: christou@chem.ufl.edu

Abstract: The preparation and properties of [Mn₄O₃(O₂CPh-R)₄(dbm)₃] (R = H, *p*-Me, *p*-OMe, and *o*-Cl; dbm⁻ is the anion of dibenzoylmethane) single-molecule magnets (SMMs) with virtual C_S symmetry are reported. They were prepared by controlled potential electrolysis in 26−80% yields. The structures comprise a distorted-cubane core of virtual C_S symmetry, in contrast to the other, more common complexes of this type with virtual C_{3V} symmetry. Solid-state magnetic susceptibility data establish the complexes have $S = 9/2$ ground-state spins, and ac susceptibility studies indicate they are single-molecule magnets (SMMs). Magnetization vs dc field sweeps below 1.00 K reveal hysteresis loops confirming a SMM, with a very large step at zero applied field diagnostic of fast quantum tunneling of magnetization (QTM) through the anisotropy barrier. The fast QTM rate suggested a significant rhombic ZFS parameter E, as expected from the low (virtual C_S) symmetry. This was confirmed by high-frequency electron paramagnetic resonance spectroscopy on polycrystalline and single-crystal studies. The results confirm the importance of symmetry on the QTM rates.

Introduction

There has been great interest during the past few years in polynuclear oxide-bridged metal complexes as a result of some of them having the ability to function as single-molecule magnets (SMMs). This behavior is due to the intrinsic, intramolecular properties of these species, and is the result of the combination of a large ground-state spin (S) value and a significant magnetic anisotropy of the easy-axis (or Ising) type, as reflected in a negative value of the axial zero-field splitting (ZFS) parameter, D. As a result, SMMs possess a significant barrier to reversal (relaxation) of their magnetization vector, and the upper limit to this barrier (U) is given by $S^2|D|$ and $(S^2 - {}^1/_4)|D|$ for integer and half-integer S values, respectively. The slow relaxation results in imaginary (out-of-phase) magnetic susceptibility (χ_M'') signals in ac studies, and in hysteresis loops in magnetization versus applied dc field sweeps.[1]

SMMs thus represent a molecular (or bottom-up) approach to nanoscale magnets, and thus differ significantly from classical (or top-down) nanoscale magnets of metals, metal alloys, metal oxides, etc. These differences include monodispersity, crystallinity, true solubility (rather than colloid formation), and a shell of organic groups that prevents close contact of the magnetic cores with those of neighboring molecules, and which can be varied using standard chemical methods. SMMs have been proposed for several potential applications, such as in high-density information storage, where each bit of information would be stored on a single molecule, and in quantum computing, where each molecule would function as a quantum bit (qubit). The latter application would take advantage of the fact that SMMs straddle the classical/quantum interface and thus exhibit both the classical properties of the macroscale and the quantum properties of the microscale. In particular, they show quantum tunneling of the magnetization (QTM), also called magnetic quantum tunneling (MQT), whereby the magnetization tunnels through the relaxation barrier rather than going over it.[2] The

† Department of Chemistry, University of Florida.
‡ Department of Physics, University of Florida.
§ Laboratoire Louis Néel-CNRS.
‖ Indiana University.

(1) (a) Tasiopoulos, A.; Vinslava, A.; Wernsdorfer, W.; Abboud, K. A.; Christou, G. *Angew. Chem.* **2004**, *43*, 2117. (b) Murugesu, M.; Habrych, M.; Wernsdorfer, W.; Abboud, K. A.; Christou, G. *J. Am. Chem. Soc.* **2004**, *126*, 4766. (c) Edwards, R. S.; Maccagnano, S.; Yang, E.-C.; Hill, S.; Wernsdorfer, W.; Hendrickson, D. N.; Christou, G. *J. Appl. Phys.* **2003**, *93*, 7807. (d) Soler, M.; Wernsdorfer, W.; Foltin, K.; Pink, M.; Christou, G. *J. Am. Chem. Soc.* **2004**, *126*, 2156. (e) Osa, S.; Kido, T.; Matsumoto, N.; Re, N.; Pochaba, A.; Mrozinski, J. *J. Am. Chem. Soc.* **2004**, *126*, 420. (f) Dendrinou-Samara, C.; Alexiou, M.; Zaleski, C. M.; Kampf, J. W.; Kirk, M. L.; Kessissoglou, D. P.; Pecoraro, V. L. *Ang. Chem. Int.* **2003**, *42*, 3763. (g) Yoo, J.; Rumberger, E. M.; Hendrickson, D. N.; Yamaguchi, A.; Ishimoto, H.; Brechin, E. K.; Christou, G. *J. Appl. Phys.* **2002**, *91*, 7155. (h) Castro, S. L.; Sun, Z.; Grant, C. M.; Bollinger, J. C.; Hendrickson, D. N.; Christou, G. *J. Am. Chem. Soc.* **1998**, *120*, 2997. (i) Boskovic, C.; Brechin, E. K.; Streib, W. E.; Folting, K.; Bollinger, J. C.; Hendrickson, D. N.; Christou, G. *J. Am. Chem. Soc.* **2002**, *124*, 3725. (j) Sangregorio, C.; Ohm, T.; Paulsen, C.; Sessoli, R.; Gatteschi, D. *Phys. Rev. Lett.* **1997**, *78*, 4645. (k) Andres, H.; Basler, R.; Blake, A. J.; Cadiou, C.; Chaboussant, G.; Grant, C. M.; Gudel, H.-U.; Murrie, M.; Parsons, S.; Paulsen, C.; Semadini, F.; Villar, V.; Wernsdorfer, W.; Winpenny, R. E. P. *Chem. Eur. J.* **2002**, *8*, 4867. (l) Brechin, E. K.; Soler, M.; Christou, G.; Helliwell, M.; Teat, S. J.; Wernsdorfer, W. *Chem. Commun.* **2003**, 1276. (m) Berlinguette, C. P.; Vaughn, D.; Canada-Vilalta, C.; Galan-Mascaras, J. R.; Dunbar, K. R. *Angew. Chem., Int. Ed.* **2003**, *42*, 1523. (n) Sokol, J. J.; Hee, A. G.; Long, J. R. *J. Am. Chem. Soc.* **2002**, *124*, 7656.

QTM thus potentially allows the molecule to exist as a quantum superposition of states, a necessary property of a qubit. This is manifested in magnetization vs dc field sweeps where the resulting hysteresis loop, the classical property of a magnet, displays steplike features due to QTM. Such QTM steps, first reported in 1996 for $[Mn_{12}O_{12}(O_2CMe)_{16}(H_2O)_4] \cdot 2MeCO_2H \cdot 4H_2O$, correspond to field positions where states on either side of the double-well potential energy surface are in resonance and therefore QTM can occur, leading to increases in the rate of magnetization relaxation.

A group of SMMs that we have been studying in great detail over the past few years is the $[Mn_4O_3X(O_2CMe)_3(dbm)_3]$ family of clusters, where $X = MeCO_2^-$, Cl^-, Br^-, N_3^-, NCO-, OH^-, MeO^-, etc., and dbm^- is the anion of dibenzoylmethane. These contain the $[Mn_4(\mu_3-O)_3(\mu_3-X)]^{6+}$ distorted-cubane core of virtual C_{3v} symmetry, are mixed-valence ($3Mn^{III}$, Mn^{IV}), possess a well-isolated ground-state spin of $S = 9/2$,[3] and display hysteresis loops containing QTM steps. Further, a second type of these complexes, of formula $[Mn_4O_3Cl_4(O_2CR)_3(py)_3]$ (R = Me, Et; py = pyridine), crystallize as head-to-head dimers and have allowed for the first time the identification of exchange-biased QTM[4] and quantum coherence in SMMs.[5]

In the present work, we have extended our study of the monomeric Mn_4 complexes to a subclass possessing a much more distorted $[Mn_4(\mu_3-O)_3(\mu_3-X)]^{6+}$ core of only virtual C_s symmetry. We report the synthesis by controlled potential electrolysis and the characterization by a variety of techniques of $[Mn_4O_3(O_2CPh-R)_4(dbm)_3]$ complexes, where R = H (**9**), *p*-Me (**10**), *p*-OMe (**11**) and *o*-Cl (**12**). These contain the low symmetry $[Mn_4(\mu_3-O)_3(\eta^2,\mu_3-O_2CPh-R)]^{6+}$ core. These complexes all still possess $S = 9/2$ ground states but their lower structural symmetry has been found to have an important effect on their resulting magnetic properties, particularly on their hysteresis loops and QTM rates. These properties will be described in detail.

Experimental Section

Syntheses. All chemicals were used as received unless otherwise stated. Abbreviations: O_2CPh = benzoate; O_2CPh-*p*-Me = 4-methylbenzoate; O_2CPh-*p*-OMe = 4-methoxybenzoate; dbmH = dibenzoylmethane. The sodium salt of dibenzoylmethane (Na(dbm).$\frac{1}{2}H_2O$), and the complexes $(NBu^n_4)[Mn_4O_2(O_2CPh)_9(H_2O)]$ (**1**), $(NBu^n_4)[Mn_4O_2(O_2CPh$-*p*-Me$)_9(H_2O)]$ (**2**), $(NBu^n_4)[Mn_4O_2(O_2CPh$-*p*-OMe$)_9(H_2O)]$ (**3**),

$(NBu^n_4)[Mn_4O_2(O_2CPh_4$-*o*-Cl$)_9(H_2O)]$ (**4**), $[Mn_4O_2(O_2CPh)_6(dbm)_2]$ and $[Mn_4O_3(O_2CMe)_4(dbm)_3]$ were prepared according to the literature methods.[3c]

$(NBu^n_4)[Mn_4O_2(O_2CPh)_7(dbm)_2]$ (5). Solid Na(dbm).$\frac{1}{2}H_2O$ (1.23 g, 5.00 mmol) was added to a stirred red solution of complex **1** (4.02 g, 2.50 mmol) in CH_2Cl_2 (145 mL). Over the course of several hours, the color of the solution changed from red-brown to dark brown. A precipitate (NaO$_2$CPh) was removed by filtration, and the filtrate was treated with a mixture of Et_2O/hexanes (200 mL, 1:1 v/v). A reddish-brown precipitate was produced, which was collected by filtration, washed with Et_2O, and dried in air; the yield was ~75%. Anal. Calcd (Found) for $C_{96.3}H_{95.6}NO_{20}Cl_{2.6}Mn_4$ (**5**·1.3CH$_2$Cl$_2$, 1898.96 g mol^{-1}): C, 60.67 (60.91): H, 5.44 (5.07); N, 0.69 (0.74).

$(NBu^n_4)[Mn_4O_2(O_2CPh$-*p*-Me$)_7(dbm)_2]$ (6). Solid Na(dbm).$\frac{1}{2}H_2O$ (0.92 g, 3.74 mmol) was added to a solution of complex **2** (3.12 g, 1.85 mmol), in CH_2Cl_2 (120 mL). After several hours, NaO$_2$CPh-*p*-Me was removed by filtration, and the filtrate was treated with Et_2O/hexanes (200 mL, 1:1 v/v) to produce a reddish-brown precipitate. This was collected by filtration, washed with Et_2O, and dried in air; the yield was ~75%. Anal. Calcd (Found) for $C_{102.5}H_{108}NO_{20}ClMn_4$ (**6**·0.5CH$_2$Cl$_2$, 1929.20 g mol^{-1}): C, 63.62 (63.82); H, 5.82 (5.64); N, 1.01 (0.73).

$(NBu^n_4)[Mn_4O_2(O_2CPh$-*p*-OMe$)_7(dbm)_2]$ (7). Solid Na(dbm).$\frac{1}{2}H_2O$ (1.18 g, 4.79 mmol) was added to a stirred solution of complex **3** (4.40 g, 2.37 mmol) in CH_2Cl_2 (165 mL). After several hours, NaO$_2$CPh-*p*-Me was removed by filtration, and the brown filtrate was treated with hexanes (200 mL) to produce a light brown precipitate. This was collected by filtration, washed with Et_2O, and dried in air; the yield was ~63%. Anal. Calcd (Found) for $C_{105}H_{113}NO_{27}Mn_4$ (**7**·hexane, 2084.92 g mol^{-1}): C, 62.26 (62.31); H, 5.85 (6.13); N, 0.67 (0.83).

$(NBu^n_4)[Mn_4O_2(O_2CPh$-*o*-Cl$)_7(dbm)_2]$ (8). Solid Na(dbm).$\frac{1}{2}H_2O$ (0.51 g, 2.10 mmol) was added to a stirred solution of complex **4** (2.00 g, 1.04 mmol) in CH_2Cl_2 (100 mL). After several hours, NaO$_2$CPh-*o*-Cl was removed by filtration, and the brown filtrate was treated with Et_2O/hexanes (200 mL, 1:1 v/v) to give a light brown precipitate. This was collected by filtration, washed copiously with Et_2O, and dried in air; the yield was ~75%. Anal. Calcd (Found) for $C_{110}H_{97}NCl_7O_{22}Mn_4$ (**8**·2hexane, 2202.01 g mol^{-1}): C, 58.36 (58.65): H, 5.22 (4.34); N, 0.64 (0.62).

$[Mn_4O_3(O_2CPh)_4(dbm)_3]$ (9). Method A. A slurry of complex **5** (1.48 g, 0.81 mol) in a 1.0 M solution of $NBu^n_4PF_6$ in MeCN (60.0 mL) was electrolyzed at 0.65 V vs Fc/Fc$^+$ under aerobic conditions at room temperature. While the current was flowing, dbmH (0.20 g, 0.89 mmol) in a 1.0 M solution of $NBu^n_4PF_6$ (12.0 mL) was added dropwise. Approximately midway through the electrolysis, a brown solid began to precipitate from the solution. When the electrolysis was complete (45−60 min), the precipitate was collected by filtration, washed with MeCN and Et_2O, and dried in air. The yield was 70−80%. Recrystallization from CH_2Cl_2/Et_2O gave well-formed, dark red-brown crystals. Anal. Calcd (Found) for $C_{73}H_{53}Mn_4O_{17}$ (**9**, 1421.99 g mol^{-1}): C, 61.66 (61.23); H, 3.76 (3.71).

Method B. To a stirred solution of $[Mn_4O_2(O_2CPh)_6(dbm)_2]$ (0.20 g, 0.14 mmol) and $NBu^n_4MnO_4$ (0.041 g, 0.11 mmol) in MeCN (35 mL) was added dropwise a solution of dbmH (0.037 g, 0.16 mmol) in MeCN (2.0 mL). After 1 h, addition of hexanes (15 mL) produced a red-brown precipitate, and this was collected by filtration, washed with Et_2O, and dried in air; the yield was 8%. The IR and NMR spectra were identical to that of material prepared by Method 1.

Method C. Solid benzoic acid (0.21 g, 1.72 mmol) was dissolved in a solution of $[Mn_4O_3(O_2CMe)_4(dbm)_3]$ (0.50 g, 0.28 mmol) in CH_2Cl_2/toluene (30 mL, 2:1 v/v). After 30 minutes, the solvent was removed by rotary evaporation to give a brown precipitate. This was dissolved in CH_2Cl_2/toluene (30 mL, 2:1 v/v), the solvent again removed, and the cycle repeated one more time. The solid was then dissolved in MeCN (30 mL), and the solution left undisturbed. Dark crystals began to form after 1 h, and when crystallization was judged complete, they

(2) Friedman, J. R.; Sarachik, M. P.; Tejada, J.; Ziolo, R. *Phys. Rev. Lett.* **1996**, *76*, 3830. (b) Thomas, L.; Lionti, L.; Ballou, R.; Gatteschi, D.; Sessoli, R.; Barbara, B. *Nature* **1996**, *383*, 145. (c) Wernsdorfer, W.; Sessoli, R. *Science* **1999**, *284*, 133. (d) Soler, M.; Wernsdorfer, W.; Folting, K.; Pink, M.; Christou, G. *J. Am. Chem. Soc.* **2004**, *126* (7), 2156. (e) Soler, M.; Wernsdorfer, W.; Abboud, K. A.; Hendrickson, D. N.; Christou, G. *Polyhedron* **2003**, *22*, 1777. (f) Sanudo, E. C.; Brechin, E. K.; Boskovic, C.; Wernsdorfer, W.; Yoo, J.; Yamaguchi, A.; Concolino, T. R.; Abboud, K. A.; Rheingold, A. L.; Ishimoto, H.; Hendrickson, D. N.; Christou, G. *Polyhedron* **2003**, *22*, 2267. (g) Canneschi, A.; Ohm, T.; Paulsen, C.; Rovai, D.; Sangregorio, C.; Sessoli, R. *J. Magn. Magn. Mater.* **1998**, *177*, 1330. (h) Zhang, X. X.; Tejada, J.; Hernandez, J. M.; Ziolo, R. F. *Nanostruct. Mater.* **1997**, *9*, 301. (i) Barbara. B.; Wernsdorfer, W.; Sampaio, L. C.; Park, J. G.; Paulsen, C.; Novak, M. A.; Ferrer, R.; Mailly, D.; Sessoli, R.; Caneschi, A.; Hasselbach, K.; Benoit, A.; Thomas, L. *J. Magn. Magn. Mater.* **1995**, *140*, 1825.

(3) (a) Bashkin, J. S.; Chang, H.-R.; Streib, W. E.; Huffman, J. C.; Hendrickson, D. N.; Christou, G. *J. Am. Chem. Soc.* **1987**, *109*, 6502. (b) Li, Q.; Vincent, J. B.; Libby, E.; Chang, H.-R.; Huffman, J. C.; Boyd, P. D. W.; Christou, G.; Hendrickson, D. N. *Angew. Chem., Int. Ed. Engl.* **1988**, *27*, 1721. (c) Wang, S.; Tsai, H.-L.; Folting, K.; Streib, W. E.; Hendrickson, D. N.; Christou, G. *Inorg. Chem.* **1996**, *35*, 7578−7589.

(4) Wernsdorfer, W.; Aliaga-Alcalde, N.; Hendrickson, D. N.; Christou, G. *Nature* **2002**, *416*, 406.

(5) Hill, S.; Edwards, R. S.; Aliaga-Alcalde, N.; Christou, G. *Science* **2003**, *302*, 1015.

were collected by filtration, washed with Et$_2$O, and dried in air; the yield was ~13%. The product was identified as complex **9** by IR and ^{1}H NMR spectroscopic comparison with material from Method A.

[Mn$_4$O$_3$(O$_2$CPh-*p*-Me)$_4$(dbm)$_3$] (10). Compound **6** (1.13 g, 0.60 mmol) was dissolved in a 1.0 M solution of NBu$^n_4$PF$_6$ in MeCN (60 mL) and electrolyzed as described for complex **9** (Method A). The applied potential was 0.63 V vs Fc/Fc$^+$, and a solution of dbmH (0.16 g, 0.71 mmol) in the same solvent was added dropwise during the electrolysis. The precipitate that formed was collected by filtration, washed with MeCN and Et$_2$O, and dried in air; the yield was 65–75%. Recrystallization from CH$_2$Cl$_2$/Et$_2$O gave well-formed, dark red-brown crystals, crystallographically identified as **10**·2CH$_2$Cl$_2$, which were collected and dried in air. Anal. Calcd (Found) for C$_{78}$H$_{63}$Cl$_2$-Mn$_4$O$_{17}$ (**10**·CH$_2$Cl$_2$, 1563.02 g mol^{-1}): C, 59.94 (59.63); H, 4.06 (4.08).

[Mn$_4$O$_3$(O$_2$CPh-*p*-MeO)$_4$(dbm)$_3$] (11). Compound **7** (0.89 g, 0.45 mmol) was dissolved in a 1.0 M solution of NBu$^n_4$PF$_6$ in MeCN (60 mL) and electrolyzed as described for complex **9** (Method A). The applied potential was 0.63 V vs Fc/Fc$^+$, and a solution of dbmH (0.16 g, 0.71 mmol) in the same solvent was added dropwise during the electrolysis. The precipitate that formed was collected by filtration, washed with MeCN and Et$_2$O, and dried in air. The yield was 45%. Anal. Calcd (Found) for C$_{78}$H$_{62.5}$N$_{0.5}$O$_{21}$Mn$_4$ (**11**.1/2MeCN, 1563.13 g mol^{-1}): C, 59.93 (59.05); H, 4.03 (4.28); N, 0.45 (0.37).

[Mn$_4$O$_3$(O$_2$CPh-*o*-Cl)$_4$(dbm)$_3$] (12). Compound **8** (1.00 g, 0.50 mmol) was dissolved in a 1.0 M solution of NBu$^n_4$PF$_6$ in MeCN (90 mL) and electrolyzed as described for complex **9** (Method A). The applied potential was 0.65 V vs Fc/Fc$^+$, and a solution of dbmH (0.11 g, 0.50 mmol) in the same solvent was added dropwise during the electrolysis. The precipitate that formed was collected by filtration, washed with MeCN and Et$_2$O, and dried in air. The yield was 26%. Anal. Calcd (Found) for C$_{73}$H$_{49}$O$_{17}$Cl$_4$Mn$_4$ (**12**, 1559.76 g mol^{-1}): C, 56.21 (55.68); H, 3.17 (3.08).

X-ray Crystallography and Structure Solution. A crystal of complex **10**·2CH$_2$Cl$_2$ of suitable size was selected from the bulk sample (maintained in mother liquor to avoid solvent loss) and mounted in a filament loop surrounded with a small amount of the liquid. The crystal was transferred to the goniostat, where it was cooled to −168 °C for characterization and data collection. Details of the diffractometry, low-temperatures facilities, and computational procedures employed by the Molecular Structure Center are available elsewhere.[6]

A preliminary search for peaks and analysis using the programs DIRAX and TRACER revealed a triclinic unit cell (*a* = 15.950(4) Å, *b* = 16.757(4) Å, *c* = 15.491(1) Å, α = 96.60(1)°, β = 99.82(1)°, γ = 64.93(1)°, Z = 2), and the choice of centrosymmetric space group P$\bar{1}$ was confirmed by the subsequent solution and refinement of the structure. Data processing gave a set of 13 029 unique intensities and R_{av} = 0.018 for the averaging of 344 of these that had been measured more than once. Four standard intensities measured every 300 reflections showed no significant trends. The limits for *h*, *k*, and *l* were −18 to +19, −19 to +19, and −18 to 0, respectively. The structure was solved by a combination of direct methods (MULTAN-78) and Fourier techniques. In addition to the Mn$_4$ complex, the asymmetric unit contains two molecules of CH$_2$Cl$_2$. Many of the hydrogen atoms were located in a difference Fourier map at the later stages of the refinement, with at least one on each of the terminal methyl groups. In the final cycles of full-matrix least-squares refinement on *F*, all of the non-hydrogen atoms were refined using anisotropic thermal parameters, while all hydrogen atoms were introduced in fixed, idealized positions with isotropic thermal parameters equivalent to 1.0 plus the isotropic equivalent of the parent atom. The final *R*(*F*) and *R*$_w$(*F*) were 0.0577 and 0.0544, respectively, for 938 variables. The full unique data set was used; however, reflections with *I* < 2.0 sigma (*I*) were given zero weight.

Physical Measurements. ^{1}H NMR spectra were collected on a 300 MHz Varian Gemini 2000 spectrometer with the protio-solvent signal

(6) http://www.chem.indiana.edu/facilities/msc_front.htm.

used as reference. Chemical shifts are quoted on the δ scale (downfield shifts are positive). IR spectra were recorded as KBr disks on a Nicolet model 510P spectrophotometer. Cyclic voltammograms and differential pulse voltammograms were recorded with a BAS CV-50 voltammetric analyzer; studies were performed on MeCN solutions containing ~1 mM analyte and 0.1 M NBu$^n_4$PF$_6$ as supporting electrolyte. The cyclic voltammograms were recorded at a scan rate of 100 mV/s. The electrodes were a glassy carbon working electrode, a platinum wire auxiliary electrode, and a reference electrode of Ag/AgNO$_3$ in MeCN or Ag/AgI/NBu$^n_4$Ag$_3$I$_4$ in CH$_2$Cl$_2$. The ferrocene/ferricinium (Fc/Fc$^+$) couple was used as an internal reference. Elemental analyses were performed at Indiana University using a Perkin-Elmer Series II CHNS/O Analyzer 2000. Magnetic data (ac and dc) were recorded on a Quantum Design MPMS-XL SQUID magnetometer equipped with a 7 T magnet and capable of operating in the 1.8–400 K temperature range. Dc magnetic susceptibility data were collected on microcrystalline samples restrained in eicosane to prevent torquing. Ac magnetic susceptibility measurements were performed in an oscillating ac field of 3.5 G and a zero dc field. The oscillation frequencies were in the 50–1488 Hz range. Diamagnetic corrections to the observed susceptibilities were applied using Pascal's constant. Magnetic studies below 1.8 K were carried out on single crystals using a micro-SQUID apparatus operating down to 0.04 K.[7] High-frequency electron paramagnetic resonance (HFEPR) studies on both powders and single crystals were performed in the 59–269 GHz frequency range using a Millimeter-wave Vector Network Analyzer (MVNA) described elsewhere.[8] Data were obtained by sweeping the magnetic field at a constant frequency and temperature. In addition, some of the fixed frequency measurements were repeated at different temperatures. Crushed crystal samples were mixed with eicosane immediately after removal from the mother liquor in order to avoid solvent loss from the microcrystallites. Likewise, single crystals were protected with vacuum grease upon removal from the mother liquor. The samples were cooled at 10 K/min under 1 atm of helium gas. Temperature control was achieved within the variable-flow cryostat belonging to a Quantum Design PPMS system.

Results and Discussion

Syntheses of (NBu$^n_4$)[Mn$_4$O$_2$(O$_2$CPh-R)$_7$(dbm)$_2$] Complexes. Previous work had established that [Mn$_4$O$_2$(O$_2$CR)$_x$-(L−L)$_y$]^n butterfly-like complexes, where L−L is a bidentate chelate, represent excellent starting materials for a variety of reactions.[9] A large number of such complexes have been prepared by this research group over the past few years with a variety of carboxylate (RCO$_2^-$) groups, and bidentate chelates L−L such as the anion of dibenzoylmethane,[7] 2,2′-bipyridine,[10] 4-imidazole-acetate,[11] picolinate,[12] and 8-hydroxyquinolinate.[13] Of particular relevance to the present work are those containing the anion of dibenzoylmethane (dbm$^-$) and aromatic carboxylate ligands, such as benzoate and its para- and ortho-substituted derivatives. Among other benefits, the many aromatic rings lead to high solubility of these Mn$_4$ starting materials in organic solvents, and this is important in the studies to be described.

(7) Wernsdorfer, W. *Adv. Chem. Phys.* **2001**, *118*, 99.
(8) Mola, M. M.; Hill, S.; Goy, P.; Gross, M. *Rev. Sci. Instrumen.* **2000**, *71*, 186.
(9) Libby, E.; Folting, K.; Huffman, J. C.; Christou, G. *J. Am. Chem. Soc.* **1990**, *112*, 5354.
(10) (a) Vincent, J. B.; Christmas, C.; Huffman, J. C.; Christou, G.; Chang H.-R.; Hendrickson, D. N. *Chem. Commun.* **1987**, 236. (b) Vincent, J. B.; Christmas, C.; Chang, H.-R.; Li, Q.; Boyd, P. D.; W. Huffman, J. C.; Hendrickson, D. N.; Christou, G. *J. Am. Chem. Soc.* **1989**, *111*, 2086.
(11) Boskovic, C.; Folting K.; Christou, G. *Polyhedron* **2000**, *19*, 2111.
(12) (a) Libby, E.; McCusker, J. K.; Schmitt, E. A.; Folting, K.; Hendrickson, D. N.; Christou, G. *Inorg. Chem.* **1991**, *30*, 3486. (b) Libby, E.; Folting, K.; Huffman, C. J.; Huffman, J. C.; Christou, G. *Inorg. Chem.* **1993**, *32*, 2549.
(13) Bouwman, E.; Christou, G.; Lobkovsky, E.; Huffman, J. C. *J. Inorg. Bichem.* **1991**, *43*, 377.
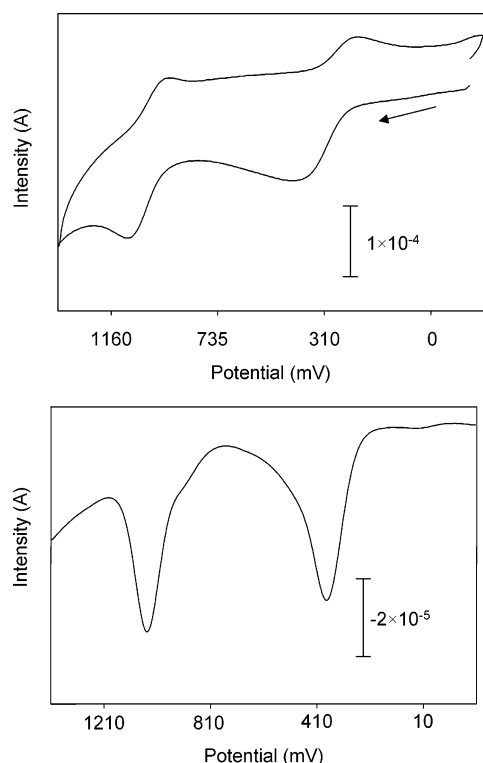
Figure 1. Cyclic voltammogram (top) and differential pulse voltammogram (bottom) of $(NBu^n_4)[Mn_4O_2(O_2CPh\text{-}p\text{-}Me)_7(dbm)_2]$ (**6**) in MeCN containing 0.1 M $NBu^n_4PF_6$.

Table 1. Oxidation Potentials for Complexes **5**−**8** in MeCN Obtained by Cyclic Voltammety ($E_{1/2}$) and Differential Pulse Voltammetry (E_{DPV})

	1st oxidation[a]		2nd oxidation[a]	
R	$E_{1/2}$	E_{DPV}	$E_{1/2}$	E_{DPV}
H (**5**)	0.44	0.41	1.10	1.10
p-Me (**6**)	0.37	0.37	1.05	1.04
p-MeO (**7**)	0.33	0.33	1.00	1.00
o-Cl (**8**)	0.54	0.51	1.22	1.19

[a] Volts vs ferrocene/ferricinium; ± 0.02 V.

The four complexes $(NBu^n_4)[Mn_4O_2(O_2CPh\text{-}R)_9(H_2O)]$ (**1**−**4**), differing only in the benzoate substituent and all available in high yield using the published procedure for the $PhCO_2^-$ derivative, are excellent starting points to access the corresponding dbm$^-$ species by reaction with 2 equiv of Na(dbm) in CH_2Cl_2 (eq 1).[14] This is a published procedure to the

$$[Mn_4O_2(O_2CPh\text{-}R)_9(H_2O)]^- + 2\ dbm^- \rightarrow$$
$$[Mn_4O_2(O_2CPh\text{-}R)_7(dbm)_2]^- + 2\ R\text{-}PhCO_2^- + H_2O \quad (1)$$
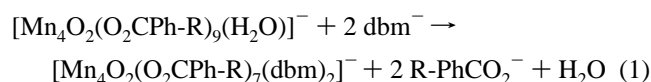
benzoate complex $(NBu^n_4)[Mn_4O_2(O_2CPh)_7(dbm)_2]$ (**5**), and it has now been successfully employed for the corresponding complexes **6** (R = p-Me), **7** (R = p-MeO) and **8** (R = o-Cl).

Electrochemical Studies on $(NBu^n_4)[Mn_4O_2(O_2CPh\text{-}R)_7$-$(dbm)_2]$ Complexes. The electrochemical properties of complexes **5**−**8** were investigated by cyclic voltammetry (CV) and differential pulse voltammetry (DPV) in MeCN. Complexes **5**−**8** display two one-electron oxidation processes at potentials in the 0.33−0.54 and 1.00−1.22 V ranges vs Fc/Fc$^+$. The scans for representative complex **6** are shown in Figure 1, and the oxidation potentials for all four compounds are listed in Table 1. As expected, the oxidation potentials reflect the electron withdrawing or donating ability of the substituents on the phenyl ring, with the Me and MeO groups giving lower oxidation potentials than benzoate, whereas the Cl substituent gives higher ones. The profile of the CV traces is consistent with a chemical change occurring after electron transfer. Thus, the ratio of forward to reverse currents, I_f /I_r is significantly less than one, and the DPV features are broader than would be expected for
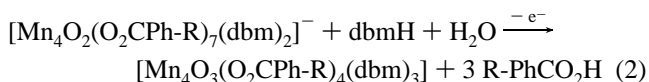
a chemically reversible process. The conclusion that the oxidized complex undergoes a structural transformation had already been established in previous work for complex **5**,[15,16] and the present results demonstrate that this is also true for complexes **6**−**8** and identifies the corresponding potentials. With this behavior established, the bulk oxidation of complexes **5**−**8** by controlled potential electrolysis was carried out.

Controlled Potential Electrolysis of Complexes 5−8. The utility of controlled potential electrolysis (CPE) of $[Mn_4O_2]^{8+}$ ($4Mn^{III}$) complexes as a synthetic route to new Mn_4 complexes had previously been established when the butterfly complexes $[Mn_4O_2(O_2CMe)_6(py)_2(dbm)_2]$ and complex **5** were oxidized by one electron and found to convert to the corresponding $[Mn_4O_3(O_2CR)_4(dbm)_3]$ (R = Me, Ph) complexes containing the $[Mn_4O_3(O_2CR)]^{6+}$ ($3Mn^{III}$, Mn^{IV}) distorted-cubane core.[15,16] This synthetic methodology was now applied to all the present complexes. MeCN was chosen as the solvent for several reasons: high solubility of the starting materials, a usable potential range, a suitably high dielectric constant and low viscosity, and poor solubility of the products, leading to their precipitation from the electrolysis solutions and consequent facile separation from the supporting electrolyte, $NBu^n_4PF_6$. Thus, complexes **5**-**8** were dissolved in MeCN containing 1.0 M $NBu^n_4PF_6$ as supporting electrolyte, and electrolyzed with an applied potential of 0.64−0.70 V vs Fc/Fc$^+$, depending on the compound. The potential was chosen so as to be ∼0.2 V greater than the DPV peak value for the first oxidation. On the basis of our previous experience of optimizing the yields of such CPE reactions,[15,16] the MeCN was not dried before use and 1 equiv of dbmH in the same solvent was added dropwise to the solution during the electrolysis. Brown precipitates slowly formed over the course of the electrolyses (45−60 min), as the insoluble products **9**−**12** slowly formed from **5**−**8**, respectively. The transformations are summarized in eq 2.

$$[Mn_4O_2(O_2CPh\text{-}R)_7(dbm)_2]^- + dbmH + H_2O \xrightarrow{-e^-}$$
$$[Mn_4O_3(O_2CPh\text{-}R)_4(dbm)_3] + 3\ R\text{-}PhCO_2H \quad (2)$$

As discussed in detail previously,[15] the overall conversion involves an oxidation-induced incorporation of a H_2O molecule into the complex, converting its core from $[Mn_4(\mu_3\text{-}O)_2]^{8+}$ to $[Mn_4(\mu_3\text{-}O)_3]^{7+}$, with carboxylate groups acting as the H^+-acceptors. This is the reason the electrolysis solvent was not dried before use. Product complexes **9**−**12** were identified by IR and ^1H NMR spectroscopy, and elemental analysis, and in

(14) Wemple, M. W.; Tsai, H.-L.; Wang, S.; Claude, J.-P.; Streib, W. E.; Huffman, J. C.; Hendrickson, D. N.; Christou, G. *Inorg. Chem.* **1996**, *35*, 6437.

(15) Wang, S.; Wemple, M. S.; Tsai, H.-L.; Folting, K.; Huffman, J. C.; Hagen, K. S.; Hendrickson, D. N.; Christou, G. *Inorg. Chem.* **2000**, *39*, 1501.
(16) Wang, S.; Tsai, H.-L.; Hagen, K. S.; Hendrickson, D. N.; Christou, G. *J. Am. Chem. Soc.* **1994**, *116*, 8376.
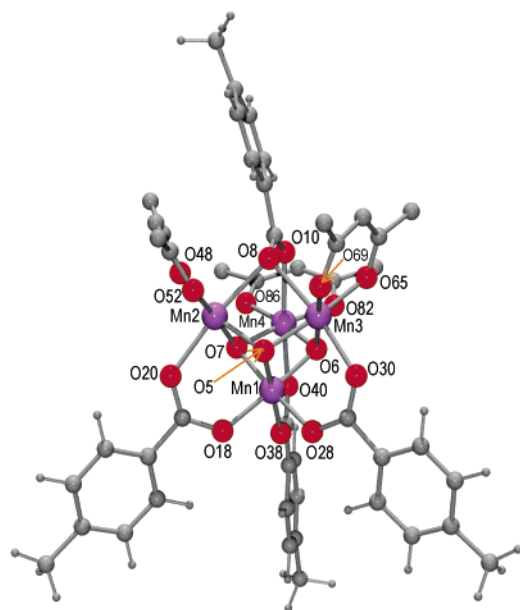
Figure 2. ORTEP plot at the 50% probability level of [Mn$_4$O$_3$(O$_2$CPh-*p*-Me)$_4$(dbm)$_3$] (**10**). For clarity, carbon atoms are represented as idealized spheres and only one phenyl carbon atom of the dbm$^-$ group is shown. Color code: Mn violet; O red; C gray.

the case of complexes **9** and **10** by X-ray crystallography. The yields were in the 65−75% range.

An obvious additional objective, given the success of the CPE method for the oxidation of manganese butterfly complexes, was a second oxidation to achieve a Mn$_4$ product at the [2Mn^{III}-2Mn^{IV}] oxidation level. Thus, the CPE was carried out on (NBu^n$_4$)[Mn$_4$O$_2$(O$_2$CPh)$_7$(dbm)$_2$] with an applied potential of 1.2 V vs Fc/Fc$^+$ under an inert (N$_2$) atmosphere in a mixture of CH$_2$Cl$_2$/MeCN; the chosen potential was 0.1 V more anodic than the second oxidation potential for this compound in Table 1, but otherwise the same procedure that yields **9** was employed. However, the only product that could isolated in a pure form from the electrolysis solution was known [Mn$_{12}$O$_{12}$(O$_2$CPh)$_{16}$-(H$_2$O)$_4$][17] in a low yield of ∼5%. It was identified by IR and ^{1}H NMR spectroscopic comparison with authentic material. This complex contains 8Mn^{III} and 4Mn^{IV} and no dbm$^-$ ligands. Our suspicion is that a second oxidation generates species with dbm$^-$ groups attached to Mn^{IV} ions, and this causes oxidation and loss of the former, leading to aggregation of the Mn$_4$ fragment to the Mn$_{12}$ product. However, the low yield implies a complicated reaction system, likely with several different species in solution, and it was not studied further.

Description of the Structure of 10. The molecular structure of [Mn$_4$O$_3$(O$_2$CPh-*p*-Me)$_4$(dbm)$_3$] (**10**) is shown in Figure 2; full listings of bond distances and angles are available as Supporting Information. Compound **10** possesses a central [Mn$_4$-(μ_3-O$_3$)(η^2,μ_3-O$_2$CPh-*p*-Me)]$^{6+}$ core that can be described as a Mn$_4$ trigonal pyramid with the Mn^{IV} ion (Mn1) at the apex, a μ_3-O^{2-} ion bridging each vertical face and a η^2,μ_3-carboxylate group bridging the basal plane. One carboxylate O atom (O8) of the latter bridges Mn2 and Mn3, whereas the other (O10) is bound terminally to Mn4. All of the manganese atoms are hexacoordinated. The metal oxidation states are supported by the
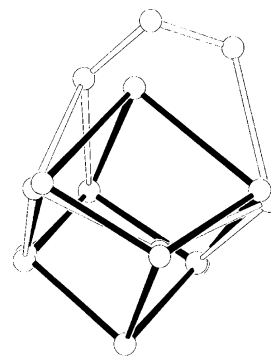
Figure 3. Structural comparison of the [Mn$_4$O$_3$X]$^{6+}$ cores with complexes with virtual C_{3v} (solid bonds) and virtual C_s (empty bonds) symmetries.

shorter average bond distances at the Mn^{IV} ion, and the presence of Jahn−Teller (JT) elongation axes at Mn2, Mn3, and Mn4, as expected for high-spin Mn^{III} in near-octahedral geometry. The JT elongation axes are those on which lie atoms O8 and O10 of the unique carboxylate group. The peripheral ligation is provided by a chelating dbm$^-$ on each Mn^{III} ion, and a *syn,-syn-μ*-carboxylate group bridging each Mn^{III}Mn^{IV} pair. Excluding the unique, central η^2,μ_3-carboxylate ligand gives virtual C_{3v} symmetry for the molecule, but the unique carboxylate lowers the virtual symmetry to C_S, with the virtual mirror plane passing through Mn1, Mn4, and O5, among others. Consequently, there are three types of Mn...Mn separations: The Mn1...Mn(2,3,4) distances (average 2.794 Å) are the shortest in the molecule, consistent with the bis-oxide-bridged nature of these Mn^{III}Mn^{IV} pairs. In contrast, the Mn^{III}...Mn^{III} separations are significantly longer and fall into two types, Mn4...Mn(2,3) (average 3.385 Å) and Mn2...Mn3 (3.1464(11) Å). The shorter latter distance is consistent with the extra mono-atomic bridge between these two Mn atoms provided by atom O8. The structures of complexes **11** and **12** are concluded to be very similar to that of **10**, on the basis of their empirical formulas and very similar IR and ^{1}H NMR spectra.

The low (virtual C_S) symmetry cores of complexes **9−12** are distinctly different from those for the much more common types of [Mn$_4$O$_3$X(O$_2$CR)$_3$(dbm)$_3$] (X = Cl$^-$, Br$^-$, F$^-$, N$_3^-$, NCO$^-$, MeCO$_2^-$, etc) complexes, which contain a single μ_3-X$^-$ ligand mono-atomically (η^1) bridging the three Mn^{III} ions and thus have virtual C_{3V} symmetry.[18] The single X$^-$ ligand lies at the intersection of the three Mn^{III} JT elongation axes. The two cores are compared in Figure 3, where it can be seen that the η^2,μ_3-carboxylate ligand in **9−12** has the effect of opening up the [Mn^{III}$_3$(μ_3-O$_2$CR)] portion of the core, and consequently the JT axes no longer intersect. We have discussed elsewhere[15] that the unusual η^2,μ_3-binding mode of the carboxylate ligands is due to the bulkiness of their benzoate group (and its substituted versions) that would cause severe steric problems with the dbm$^-$ groups should the central carboxylate group bridge in the same η^1,μ_3-mode as the X$^-$ groups in the C_{3V} symmetry complexes. The more open structure of **9−12** has an important effect on the magnetic properties of **9−12**, as will be discussed later.

^{1}H NMR Spectroscopic Studies. NMR spectroscopy is a very useful way of probing the structures of manganese

(17) Sessoli, R.; Tsai, H.-L.; Schake, A. R.; Wang, S.; Vincent, J. B.; Folting, K.; Gatteschi, D.; Christou, G.; Hendrickson, D. N. *J. Am. Chem. Soc.* **1993**, *115*, 1804.

(18) (a) Aromí, G.; Wemple, M. W.; Aubin, S. J.; Folting, K.; Hendrickson, D. N.; Christou, G. *J. Am. Chem. Soc.* **1998**, *120*, 5850. (b) Aromí, G.; Bhaduri, S.; Artus, P.; Folting, K.; Christou, G. *Inorg. Chem.* **2002**, *41*, 805.
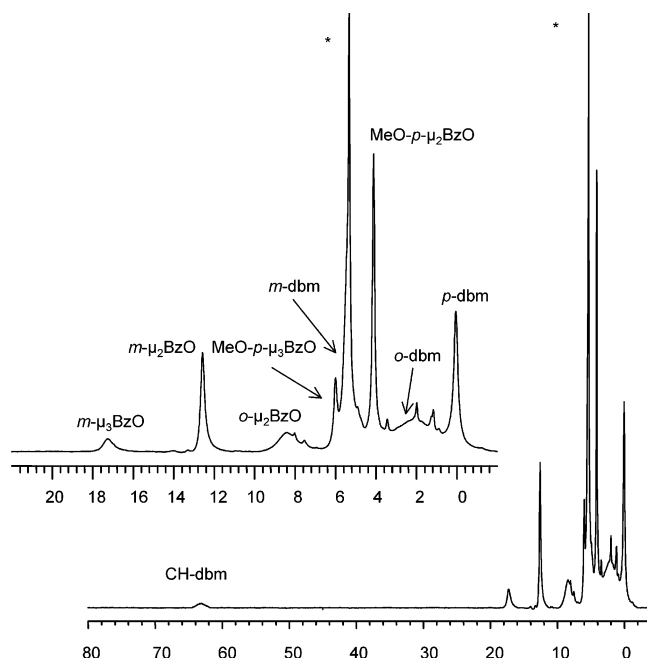
Figure 4. ¹H NMR spectrum of [Mn₄O₃(O₂CPh-*p*-OMe)₄(dbm)₃] (**11**) in CD₂Cl₂ at ~23 °C. Solvent impurity peaks are marked with an asterisk.

Table 2. ¹H NMR Spectral Data^a for Complexes **9–12**

|	R–PhCO₂⁻			dbm⁻			
R	*o*	*m*	*p*	*o*	*m*	*p*	–CH–
H (**9**)^b	8.5	13.4	7.4	2.0	5.3	−0.2	65.5
	n.o.	18.7	−2.8				
p-Me (**10**)^b	8.2	13.1	2.6	2.1	5.3	−0.1	64.0
	n.o.	18.3	15.5				
p-MeO (**11**)^b	8.4	12.5	4.1	2.1	5.3	0.1	63.6
	n.o.	17.2	6.0				
o-Cl (**12**)^b	9.2	13.6	3.5	2.0	4.8	−0.8	72.0
	n.o.	17.8	−2.4				

^{a} In CD₂Cl₂ at ~23 °C; n.o. = not observed, or assignment precluded by poor resolution. ^{b} The first and second rows for each complex give carboxylate data for the μ-(O₂CPh−R) and μ_3-(O₂CPh−R) groups, respectively.

complexes in solution[19] and establishing, for example, whether the solid-state structure is retained on dissolution. We have therefore carried out such studies on complexes **9–12** in CD₂-Cl₂ by variable temperature ¹H NMR spectroscopy.

The spectrum obtained for complex **11** at ~23 °C is shown in Figure 4. The resonances span a wide range of ~70 ppm as a result of the paramagnetic nature of the molecule. The peak assignments were made on the basis of comparisons with the spectra of related Mn₄ complexes containing acetate and deuterated acetate ligands studied previously,[15,18] peak broadnesses and relative integrations, differences between the spectra of **9–12**, and spin−lattice (T_1) relaxation time measurements. All four complexes **9–12** display very similar spectral profiles, subject to the variations in the substituents on the phenyl ring; in particular, the o-Cl substituent complicates the assignment of the phenyl resonances for complex **12**. Table 2 lists the measured chemical shifts for these complexes; a figure showing their spectra at the same temperature is provided as Supporting Information.

(19) Hendrickson, D. N.; Christou, G.; Schmitt, E. A.; Libby, E.; Bashkin, J. S.; Wang, S.; Tsai, H.-L.; Vincent, J. B.; Boyd, P. D. W.; Huffman, J. C.; Folting, K.; Li, Q. Streib. W. E. *J. Am. Chem. Soc.* **1992**, *114*, 2455.

The virtual symmetry of the molecules (assuming fast rotation of phenyl rings) is C_s. However, examination of spectra such as that in Figure 4 indicates that the effective solution symmetry is C_{3v}. Thus, the dbm⁻ groups are all equivalent, and the carboxylate groups fall into only two types, the three that are doubly bridging on the periphery of the molecule, and the unique triply bridging one in the core. A fluxional process is clearly operative that serves to increase the effective solution symmetry, and this is almost certainly a fast rotation of the unique carboxylate group about its local C_2 symmetry axis (approximately collinear with the virtual C_3 axis of the rest of the molecule). Such a process would have to occur rapidly on the ¹H NMR time scale, and this is reasonable, given that the necessary breaking and forming of Mn−O bonds involving this carboxylate group can occur in a concerted fashion, and that all these Mn−O bonds are JT elongated and weakened; a relatively low activation energy is thus likely. The proposed process is depicted in the Scheme, showing the Mn$^{III}_3$ face and an edge-on view of the triply bridging carboxylate, with all atoms except its O atoms omitted for clarity.
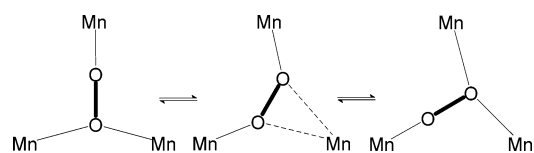
Since the remainder of the molecule has virtual C_{3V} symmetry, a fast rotation of the unique carboxylate would result in C_{3V} effective solution symmetry for these molecules, and thus the NMR spectra observed.

We also carried out variable-temperature studies on all complexes to probe whether the fluxional process could be slowed to the point of seeing decoalescence of peaks corresponding to C_S symmetry. The low solubility of **9–12** in organic solvents required the use of CD₂Cl₂, and the lowest temperature employed was thus −90 °C. However, even at this lowest temperature, the ¹H NMR spectra did not show any decoalescence, only some slight broadening from viscosity effects. This shows that the dynamic process involving the μ_3-benzoate groups is still fast on the ¹H NMR time scale even at −90 °C, indicating the activation energy barrier to be very small, as expected from the nature of the process.

Direct Current Magnetic Susceptibility Studies. Variable-temperature magnetic susceptibility measurements were performed on powdered polycrystalline samples of complexes **9–12**, restrained in eicosane to prevent torquing, in a 10 kG field and in the 2.0−300 K range. The data are shown as $\chi_M T$ vs T plots in Figure 5.

The value of $\chi_M T$ for complex **9** increases from 8.16 cm³ mol⁻¹ K at 300 K to a maximum of 11.61 cm⁻³ mol⁻¹ K at 25 K and then decreases to 5.25 cm⁻³ mol⁻¹ K at 2.0 K. Complex **10** exhibits similar behavior, with $\chi_M T$ increasing from 9.09 cm⁻³ mol⁻¹ K at 300 K to a maximum of 11.91 cm⁻³ mol⁻¹ *K* at 30 K, and then decreasing to 5.30 cm³ mol⁻¹ K at 2.0 K. For complex **11**, $\chi_M T$ increases from 8.28 cm³ mol⁻¹ K at 300 K to a maximum of 11.03 cm³ mol⁻¹ K at 30 K, and then decreases to 5.05 cm³ mol⁻¹ K at 2.0 K. Finally, complex **12** shows an increase in $\chi_M T$ from 8.72 cm³ mol⁻¹ K at 300 K to a maximum at 11.89 cm³ mol⁻¹ K at 30 K, followed by a decrease to 5.38 cm³ mol⁻¹ K at 2.0 K. The maximum $\chi_M T$ for each of the four
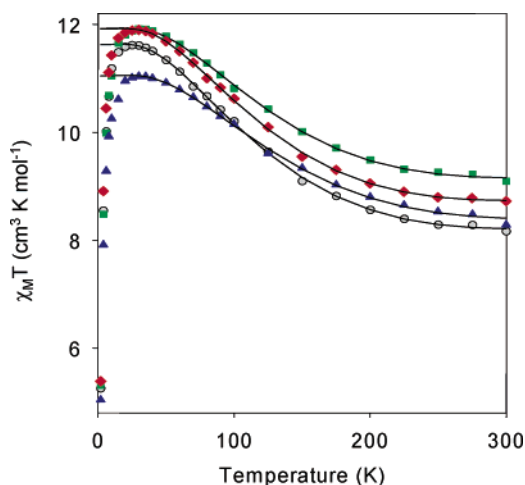
Figure 5. Plots of $\chi_M T$ *vs* T for polycrystalline samples of complexes **9** (●), **10** (■), **11** (▲), and **12** (◆) in a 10 kG field. The solid lines are the fits of the data to the theoretical expression; see the text for details and the fit parameters.

complexes is slightly below the spin-only ($g = 2$) value expected for a complex with a $S = 9/2$ ground state (12.38 cm³ mol⁻¹ K), and this is consistent with $g < 2.0$, as expected for Mn. The decrease in the $\chi_M T$ value at the lowest temperatures is likely due to zero-field splitting (ZFS), Zeeman effects from the applied field, and any weak antiferromagnetic exchange interactions. At higher temperatures, the decrease in $\chi_M T$ is due to the thermal population of excited states with $S < 9/2$.

To determine the Mn_2 pairwise exchange interactions within the molecule, the $\chi_M T$ vs T data for complexes **9**−**12** were fit to the appropriate theoretical expression. The virtual C_S symmetry in the solid state of these compounds requires four exchange parameters (J). The isotropic Heisenberg spin Hamiltonian for this C_S symmetry is given in eq 3, where J_1/J_1' and

$$\mathscr{H} = -2J_1(\hat{S}_1 \cdot \hat{S}_2 + \hat{S}_1 \cdot \hat{S}_3) - 2J_1'\hat{S}_1 \cdot \hat{S}_4 - 2J_2\hat{S}_2 \cdot \hat{S}_3 - \\ 2J_3(\hat{S}_2 \cdot \hat{S}_4 + \hat{S}_3 \cdot \hat{S}_4) \quad (3)$$

J_2/J_3 refer to the exchange interactions for $Mn^{III}Mn^{IV}$ and Mn^{III}-Mn^{III} pairs, respectively. There are thus two symmetry non-equivalent $Mn^{III}Mn^{IV}$ parameters (J_1 and J_1'), and two non-equivalent $Mn^{III}Mn^{III}$ parameters (J_2 and J_3). A full matrix diagonalization approach for obtaining the eigenvalues of this spin Hamiltonian would require diagonalization of a 500×500 matrix. Unfortunately, the convenient equivalent operator approach, based on the Kambe vector coupling method,[20] is not possible for this C_S symmetry. However, a very reasonable simplifying approximation is possible by taking $J_1 = J_1'$ as described elsewhere;[15,21] these interactions are likely very similar since both pathways involve very similar $[Mn_2(\mu\text{-}O^{2-})_2]^{3+}$ rhombs. The spin Hamiltonian now becomes that given by eq 4, for which the Kambe approach is applicable.

$$\mathscr{H} = -2J_1(\hat{S}_1 \cdot \hat{S}_2 + \hat{S}_1 \cdot \hat{S}_3 + \hat{S}_1 \cdot \hat{S}_4) - 2J_2\hat{S}_2 \cdot \hat{S}_3 - 2J_3(\hat{S}_2 \cdot \hat{S}_4 + \\ \hat{S}_3 \cdot \hat{S}_4) \quad (4)$$

Using the substitutions $\hat{S}_A = \hat{S}_2 + \hat{S}_3$, $\hat{S}_B = \hat{S}_A + \hat{S}_4$, and $\hat{S}_T = \hat{S}_B + \hat{S}_1$, where S_T is the spin of the complete molecule, allows

(20) Kambe, K. *J. Phys. Soc. Jpn.* **1950**, *5*, 48.
(21) Aliaga, N.; Folting, K.; Hendrickson, D. N.; Christou, G. *Polyhedron* **2001**, *20*, 1273.

Table 3. Exchange Parameters and g-values for Complexes **9**−**12**

R	$J_1{}^{a,b}$	$J_2{}^{a,c}$	$J_3{}^{a,d}$	g	$E(7/2)^{a,e}$
H (**9**)	−27.4	3.2	0.5	1.94	88.2
	−23.8^c	3.6^f	−	2.03^f	
p-Me (**10**)	−22.9	4.8	4.9	1.96	126.7
	−23.1^c	5.0^f	−	2.07^f	
p-MeO (**11**)	−25.3	3.3	8.1	1.89	134.7
o-Cl (**12**)	−24.7	3.5	3.4	1.96	114.9

^{a} cm⁻¹. ^{b} esd = 1.0. ^{c} esd = 2.2. ^{d} esd = 2.5. ^{e} Energy of the $S_T = 7/2$ first excited state above the ground state. ^{f} Fit parameters using a two-J model, with $J = J_1$ and $J_a = J_2 = J_3$.

the spin Hamiltonian of eq 4 to be converted to the equivalent form

$$\mathscr{H} = -J_1(\hat{S}_T{}^2 - \hat{S}_B{}^2 - \hat{S}_1{}^2) - J_2(\hat{S}_A{}^2 - \hat{S}_2{}^2 - \hat{S}_3{}^2) - \\ J_3(\hat{S}_B{}^2 - \hat{S}_A{}^2 - \hat{S}_4{}^2) \quad (5)$$

of eq 5. The eigenvalues of this Hamiltonian are then given by eq 6, where constant terms contributing to all states have been omitted.

$$E(S_T) = -J_1[S_T(S_T + 1) - S_B(S_B + 1)] - J_2[S_A(S_A + 1)] - \\ J_3[S_B(S_B + 1) - S_A(S_A + 1)] \quad (6)$$

For complexes **9**−**12**, $S_1 = 3/2$ and $S_2 = S_3 = S_4 = 2$, and the overall multiplicity of the spin system is 500, made up of 70 individual spin states ranging from $S_T = 1/2$ to 15/2.

A theoretical $\chi_M T$ vs T expression was derived using the S_T values, their energies $E(S_T)$, and the Van Vleck equation, and this expression was used to fit the experimental data. Data below 30 K were omitted because the low-temperature decrease is caused by factors not included in the above model. The fit parameters were J_1, J_2, J_3 and g. A temperature-independent paramagnetism (TIP) term was included, held fixed at 600×10^{-6} cm³ mol⁻¹. Good fits were obtained for all four compounds, and these are shown as the solid lines in Figure 5. The fit parameters are collected in Table 3. Since the J_2 and J_3 values are similar, we also fit the data for **9** and **10** to the two-J model appropriate for C_{3V} symmetry i.e., $J_1 = J$ and $J_2 = J_3 = J_a$. Good fits were again obtained (Table 3) although the g value was slightly greater than 2.0, no doubt reflecting the only approximate appropriateness of the C_{3V} model.

Comparison of the obtained results shows that the exchange interactions are very similar in the four complexes, as expected given the only small differences in the carboxylate ligands; the primary pathways for the superexchange interactions between Mn ions are via the bridging oxide ions. The $Mn^{III}Mn^{IV}$ and $Mn^{III}Mn^{III}$ interactions are antiferromagnetic and ferromagnetic, respectively, and fall within (or very near to) the ranges previously observed for the structurally related $[Mn_4O_3X\text{-}(O_2CR)_3(dbm)_3]$ (X = Cl⁻, Br⁻, F⁻, N₃⁻, NCO⁻, MeCO₂⁻, etc) complexes of -30 ± 3 cm⁻¹ and $+5 \pm 3$ cm⁻¹, respectively.[15] As already mentioned, these Mn_4 complexes have a single μ_3-X⁻ ligand mono-atomically (η^1) bridging the three Mn^{III} ions (Figure 3), and a higher virtual symmetry of C_{3V}. Thus, the structural distortions imparted by the η^2-bridging carboxylate groups in **9**−**12** have little consequence to the magnetic properties. Note that the ferromagnetic coupling between two Mn^{III} ions bridged by one μ_3-oxide and one μ_3-X⁻ (X = Cl or
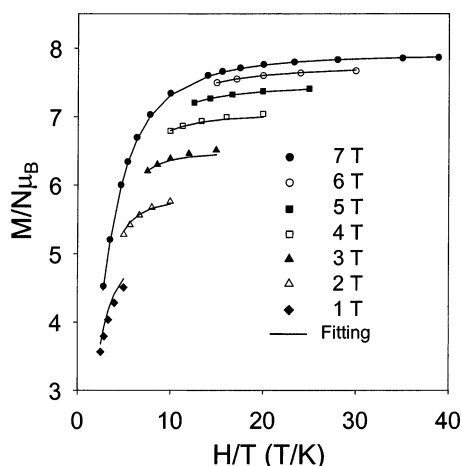
Figure 6. Plot of reduced magnetization ($M/N\mu_B$) vs H/T for complex **11** at the indicated applied dc field strengths. The solid lines are the fit of the data by the method described in the text; see the text for the fit parameters.

Br) has also been found in the [$Mn_6O_4X_4(dbm)_6$] (X = Cl or Br) complexes.[22]

The obtained J values establish that all four complexes have an $S_T = 9/2$ ground state, the $|S_T, S_A, S_B\rangle = |9/2, 4, 6\rangle$ state, which is very isolated from the nearest excited state. This ground state corresponds to the three S = 2 Mn^{III} spins being aligned parallel to give a resultant $S_B = 6$, which is aligned antiparallel to the S = 3/2 Mn^{IV} spin to give an $S_T = 9/2$ total spin. The first excited state is $S_T = 7/2$, resulting from an $S_B = 5$ resultant aligned antiparallel to the S = 3/2 Mn^{IV} spin.

For **10** and **12**, there is insignificant difference between J_2 and J_3 (Table 3), whereas for **9** and **11**, there is a slightly bigger difference. This is likely due to a combination of (i) true J_2/J_3 differences arising from different structural distortions in the cores of these complexes as a result of differing solid-sate packing forces, and (ii) a greater experimental uncertainty (i.e., a fitting 'softness') in the fit values of J_2 and J_3 compared with the much stronger J_1, which dominates the spin state energies. This is clearly apparent in the esd's of Table 3, and also in the fitting error surface vs J_1 and J_a (= J_2 = J_3) (see Supporting Information), which shows a steep-sided (i.e., well-defined) fitting minimum vs J_1, but a much shallower minimum vs J_a corresponding to a greater uncertainty. Note also that J_2 and J_3 values cause the calculated energy gap to the $S_T = 7/2$ first excited state for **9** to be significantly smaller than those for **10**– **12**, and this is consistent with the faster decrease in the $\chi_M T$ vs T plot for **9** as the first excited state gets progressively more populated at a faster rate with increasing temperature.

Magnetization versus dc Magnetic Field Studies. To confirm the $S_T = 9/2$ ground-state spin and to determine the magnitude of the zero-field splitting parameter D, magnetization vs dc field measurements were made for restrained samples of **9**–**12** at applied magnetic fields and temperatures in the 10– 70 kG and 1.8–2.5 K ranges, respectively. The data for complex **11** are shown in Figure 6 as reduced magnetization ($M/N\mu_B$) vs H/T plots, where M is the magnetization, N is Avogadro's number, μ_B is the Bohr magneton, and H is the magnetic field. For complexes populating only the ground state and possessing no axial zero-field splitting (ZFS), i.e., $D = 0$, the magnetization

versus field plot follows the Brillouin function and the isofield lines all superimpose and saturate at a value of gS. However, the experimental data of complex **11** in Figure 6 clearly do not superimpose, indicating significant magnetic anisotropy (zero-field splitting) in the ground state. Identical behavior was found for all four complexes **9**–**12**.

The data were fit to a model that assumes only the ground state is populated, includes axial zero-field splitting ($D\hat{S}_z^2$) and the Zeeman interaction, and incorporates a full powder-average. To calculate the magnetization for a polycrystalline powder sample, a suitable averaging of the magnetization must be carried out. In the case of low magnetic fields and high temperatures, where M is a linear function of field H, this entails simply numerically averaging the three principal values M_x, M_y, and M_z. In the region of high fields and low temperatures, a true powder-average of M for all orientations must be made[23] using eq 7. In this equation, θ and

$$\bar{M} = \frac{-N}{4\pi} \int_{\theta=0}^{\pi} \int_{\phi=0}^{2\pi} \left[\sum_i \left(\frac{\delta E_i}{\delta H} \right) \exp(-E_i/kT) / \right.$$
$$\left. \sum_i \exp(-E_i/kT) \right] \sin\theta \, d\theta d\phi \quad (7)$$

ϕ are the polar angle orientations of the field with respect to the molecular principal axis system, N is Avogadro's number, and $\delta E_i/\delta H$ is the change in the energy of the ith level in response to a change in a magnetic field. The energies of the various spin sublevels of the ground state S_T are obtained by diagonalization of the ($2S_T+1$)($2S_T+1$) spin Hamiltonian matrix, including the Zeeman terms, and the derivatives of the energy with respect to the magnetic field are calculated from the corresponding eigenvectors by using the Hellmann–Feynman theorem.[24]

The program MAGNET[25] was employed to fit the experimental data to those calculated using the above procedure for different values of S, D and g. The best fit for **11** is shown as the solid lines in Figure 6; the fits for the other compounds were of comparable quality. The fit parameters were $S = 9/2$ for all compounds, and D/g values of -0.60 cm^{-1}/1.95 for **9**, -0.62 cm^{-1}/ 1.92 for **10**, -0.62 cm^{-1}/1.89 for **11**, and -0.65 cm^{-1}/1.96 for **12**.

To ensure that the global fitting minimum had been obtained, root-mean-square fitting error surfaces were generated as a function of g and D, and that for representative complex **11** is provided in Supporting Information as a 2-D contour plot. As is usually the case, good fits could be found for both positive and negative D values, and this is the case also for **11**. However, the fit with negative D was nevertheless clearly superior. Further, only one fitting minimum was observed in this parameter space (with negative D), and we conclude that we have indeed identified the global minimum. In addition, the fit has a hard minimum i.e., it is well defined, in contrast to the shallower minimum with positive D. However, it should be noted that the fitting model only incorporates axial anisotropy (ZFS) and thus assumes the rhombic or transverse anisotropy (i.e., the rhombic ZFS parameter E) is zero. While this is a good

(22) Aromí, G.; Knapp, M. J.; Claude, J.-P.; Huffman, J. C.; Hendrickson, D. N.; Christou, G. *J. Am. Chem. Soc.* **1999**, *121*, 5489.

(23) Boyd, P. D. W.; Martin, R. L. *J. Chem. Soc., Dalton Trans.* **1979**, 92. (b) Gerloch, M.; McMeeking, R. F. *J. Chem. Soc., Dalton Trans.* **1975**, 2443.
(24) Bader, R. F. W.; Jones, G. A. *Can. J. Chem.* **1963**, *41*, 255.
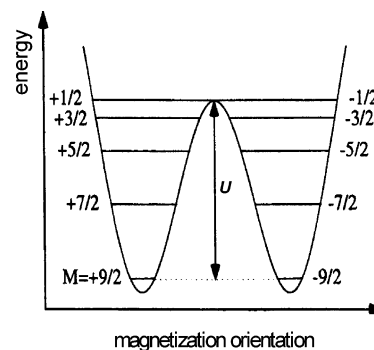(25) MAGNET, Davidson, E. R., Indiana University, Bloomington, IN.

approximation for most of the $[Mn_4O_3X(O_2CR)_3(dbm)_3]$ family of compounds with virtual C_{3V} (i.e., axial) symmetry, it is clearly less appropriate for the more distorted virtual C_S symmetry complexes **9−12** in this work. These are likely to have a significant E parameter. The fits of magnetization vs H and T data, as above, are not very sensitive to E, and we therefore held E fixed at zero. Thus, we estimate that the D values obtained from the above fits are less reliable than those for the virtual C_{3V} complexes, with a likely uncertainty of ± 0.05 cm^{-1}. For more reliable determinations of D (and E), a more sensitive technique such as EPR spectroscopy is required (vide infra).

Even given the above greater uncertainty in the D values, it is clear that the latter for complexes **9−12** are significantly greater than those for the analogous complexes with virtual C_{3V} symmetry, whose values are typically in the 0.38−0.53 cm^{-1} range. This is qualitatively as expected, given that the molecular D value in this family of Mn_4 complexes results from the projections onto the molecular anisotropy axis of the single-ion anisotropies of the three Jahn−Teller distorted Mn^{III} ions; these are the main source of the molecular anisotropy, since Mn^{IV} is a fairly isotropic ion. In the C_{3V} symmetry $[Mn_4O_3X(O_2CR)_3(dbm)_3]$ molecules, the three JT elongation axes, which are the single-ion anisotropy axes, meet at the mono-atomically bridging atom of the X^- group (Figure 3). As a result, the average angle (θ) between the three JT elongation axes and the molecular anisotropy axis (i.e., the virtual C_3 axis) is ~54° for small atoms (O, F), 45.1° for Cl, and 42.5° for Br, the difference reflecting the longer Mn−X bonds and thus a slight opening up of the $[Mn^{III}_3(\mu_3\text{-}X)]$ face of the molecule.[3,15] The decreasing θ thus represents an increasing projection of the single-ion anisotropy onto the molecular anisotropy axis (because the projection is a function of cosθ), and this rationalizes the greater D value for the Cl$^-$ and Br$^-$ complexes (−0.529 and −0.502 cm^{-1}, respectively) compared with the F$^-$ and MeCO$_2^-$ complexes (−0.379 and −0.469 cm^{-1}, respectively). Other differences between the complexes in their transverse anisotropy parameter E and fourth order anisotropy terms rule out a simple, linear correlation between θ and D. For the lower symmetry complexes **9−12**, the much greater opening up of the $[Mn^{III}_3(\mu_3\text{-}X)]$ face of the molecule (Figure 3) will lead to a significantly greater projection of the single-ion anisotropies onto the molecular anisotropy axis, and thus a larger D value, as seen.

The $[Mn_4O_3X(O_2CR)_3(dbm)_3]$ family of complexes with mono-atomically bridging X^- ligands and virtual C_{3V} symmetry have been found to be single-molecule magnets (SMMs) as a result of their $S_T = 9/2$ ground states and significant D values.[26] Since the lower symmetry Mn_4 complexes **9−12** retain both these properties, it was considered likely that they might consequently also have a significant barrier to magnetization relaxation (U) and be SMMs. This is the barrier for relaxation between the $M_S = \pm 9/2$ levels, and is shown in the potential energy double-well plot of Figure 7. As mentioned in the Introduction, the upper limit to this barrier is given by $U = (S^2 - {}^1/_4)|D|$ for a half-integer spin system, or $20|D|$ for $S = 9/2$, although the actual or effective barrier (U_{eff}) is significantly less

(26) (a) Aubin, S. M. J.; dilley, N. R.; Pardi, L.; Krzystek, J.; Wemple, M. W.; Brunel, L.-C.; Maple, M. B.; Christou, G.; Hendrickson, D. N. *J. Am. Chem. Soc.* **1998**, *120*, 4991. (b) Aubin, S. M. J.; Wemple, M. W.; Adams, D. M.; Tsai, H.-L.; Christou, G.; Hendrickson, D. N. *J. Am. Chem. Soc.* **1996**, *118*, 7746.

Figure 7. Double-well potential energy plot for an $S = 9/2$ molecule with axial symmetry and easy-axis type anisotropy. The barrier (U) to magnetization relaxation between the $M_S = \pm 9/2$ states is given by $(S^2 - {}^1/_4)|D|$.
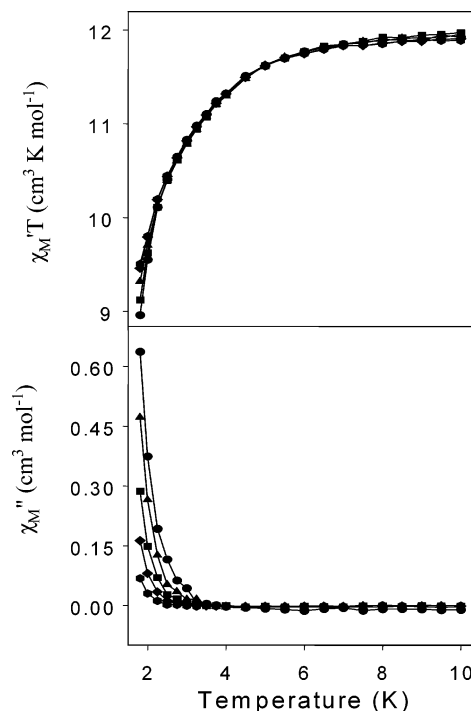
Figure 8. Ac susceptibility of complex **10** in a 3.5 G field oscillating at 99.7 (●), 250 (◆), 497 (■), 999 (▲), and 1488 (●) Hz: (top) in-phase signal (χ_M') plotted as $\chi_M'T$ vs T; and (bottom) out-of-phase signal χ_M'' vs T.

due to quantum tunneling of the magnetization (QTM) through the barrier via higher energy M_S levels. We thus decided to investigate the magnetization dynamics of these complexes using ac magnetic susceptibility studies.

Alternating Current Magnetic Susceptibility Studies. Ac studies were performed in the 1.8−10 K range using a 3.5 G ac field oscillating at frequencies in the 99.7−1488 Hz range. The results for representative complex **10** are shown in Figure 8. If the magnetization vector can relax fast enough to keep up with the oscillating field, then there is no imaginary (out-of-phase) susceptibility signal (χ_M''), and the real (in-phase) susceptibility (χ_M') is equal to the dc susceptibility. However, if the barrier to magnetization relaxation is significant compared to thermal energy (kT), then there is a nonzero χ_M'' signal and the in-phase signal decreases. In addition, the χ_M'' signal will be frequency-dependent. Such frequency-dependent χ_M'' signals are a characteristic signature of the superparamagnetic-like properties of a SMM (but by themselves do not prove the presence of a SMM). For all the complexes **9−12**, there is a

plateau at >6 K in the in-phase χ_M' signal, when plotted as $\chi_M'T$, at a value in the $11-12$ cm^3 K mol^{-1} range (consistent with a well-isolated $S = 9/2$ ground state and $g < 2$) and no out-of-phase χ_M'' signal. At lower temperatures, the in-phase signal decreases and a frequency-dependent χ_M' signal appears, suggestive of the slow relaxation of a single-molecule magnet. However, the peak maxima clearly lie at temperatures below 1.8 K, the operating limit of our instrument.

Similar frequency-dependent ac signals have been previously observed for the $[Mn_4O_3X(O_2CR)_3(dbm)_3]$ complexes with virtual C_{3V} symmetry, but in those cases the χ_M'' signals occur at higher temperatures and their peaks are observable at $1.8-2.5$ K for the higher oscillation frequencies. This might at first glance appear to be counter-intuitive, because the χ_M'' signals being at lower temperatures for the lower symmetry complexes would ostensibly suggest smaller relaxation barriers for these complexes, and yet they have the larger D values and thus the larger values of relaxation barrier U ($= (S^2 - 1/4)|D|$). However, as stated earlier, U merely represents the upper limit to the relaxation barrier. The actual or effective barrier U_{eff} will often be considerably less than U due to quantum tunneling of the magnetization (QTM) through the anisotropy barrier via higher-lying M_S levels of the $S = 9/2$ spin manifold. Thus, it is not accurate to conclude that the magnitude of the effective barriers U_{eff} will be determined merely by the D value. We shall return to this point later.

Regardless of the exact position of the χ_M'' signals in Figure 8, it is clear that their presence suggests (but does not prove) that these low-symmetry variants of the Mn$_4$ family are also single-molecule magnets (SMMs), as are the higher symmetry ones with virtual C_{3V} symmetry. To confirm this, however, studies at temperatures < 1.8 K were necessary, and these were carried out on single crystals of representative complex **9** down to 0.04 K using a micro-SQUID instrument.[7]

Magnetization versus dc Field Hysteresis Loops. Shown in Figure 9 are the results of magnetization (*M*) vs applied dc field scans of complex 9, at (i) a 0.028 T/s field sweep rate and temperatures in the $0.04-1.0$ K range (Figure 9, top); and (ii) at 0.04 K and field sweep rates in the $0.004-0.056$ T/s range (Figure 9, bottom). Hysteresis loops were observed, establishing that these virtual C_S symmetry Mn$_4$ complexes are SMMs. However, the clearly dominating feature of the hysteresis loops in Figure 9 is the large step at zero field, which indicates that quantum tunneling in zero field is so fast (corresponding to ~75% reversal of the magnetization) that there appears to be no coercivity at $M/M_S = 0$. However, at other positions, the coercivity can be seen to be temperature and time (sweep rate) dependent, increasing with decreasing temperature and increasing sweep rate, as expected for the superparamagnet-like behavior of a SMM.

Steps at periodic values of applied field are a diagnostic signature of resonant QTM, and have been seen for several distinct classes of SMMs, such as the Mn$_{12}$ family in three oxidation states (i.e., the $[Mn_{12}O_{12}(O_2CR)_{16}(H_2O)_4]^z$ ($z = 0, 1-, 2-$) complexes[17,27]), Fe$_8$,[28] and the Mn$_4$ complexes with C_{3V} virtual symmetry.[15-19] In all cases, the first step in sweeping the field from one saturating value to the other occurs at zero field where the potential energy double-well is symmetric and M_S levels on one side of the barrier are degenerate (in resonance) with those on the other side. The only exception to this is in
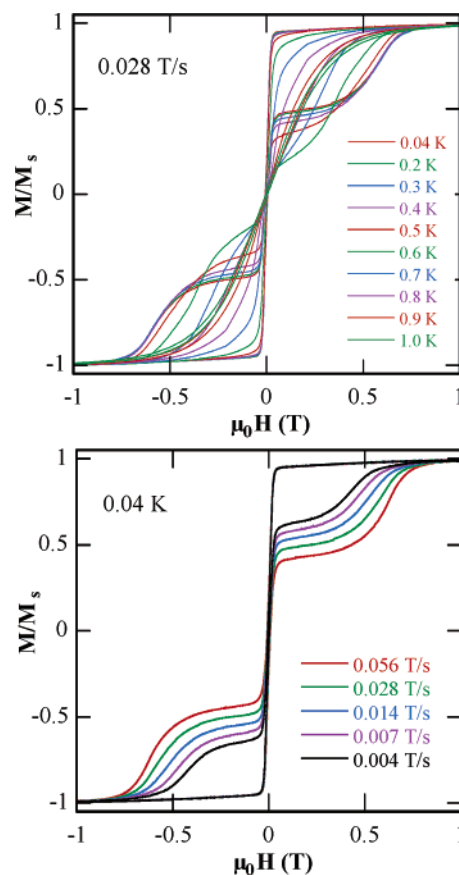
Figure 9. Magnetization (*M*) vs dc field hysteresis loops for a single crystal of **9** at the indicated temperatures and a fixed field sweep rate of 0.028 T/s (top), and at the indicated field sweep rates and a fixed temperature 0.04 K (bottom). The magnetization is normalized to its saturation value, M_S.

the small sub-group of Mn$_4$ complexes that crystallize as $[Mn_4]_2$ dimers of S_6 symmetry, where the intra-dimer exchange interaction represents a bias-field that shifts the first QTM step away from zero field.[5]

At such low temperatures, there is not enough thermal energy to overcome the potential energy barrier, and essentially all magnetization relaxation is by QTM involving a two-phonon Orbach process via higher-lying M_S levels where the tunneling rates are faster. However, Figure 9 shows that the hysteresis loops become essentially temperature-independent below approximately 0.4 K, indicating only ground-state QTM from the lowest-lying $M_S = -9/2$ level to the $M_S = +9/2$ is occurring below this temperature.

The spin Hamiltonian describing this system to second order is given by eq 8, where D is the uniaxial anisotropy (ZFS) parameter, E is the rhombic anisotropy parameter, $\hat{S}_i$ is the spin projection operator along the i ($= x, y, z$) axis, μ_B is the Bohr magneton, g is the Landé factor

$$\mathrm{H} = D\hat{S}_z^2 + E(\hat{S}_x^2 - \hat{S}_y^2) + \mu_0 g \mu_B \hat{S} \cdot H \qquad (8)$$

and $\mu_0 H$ is the applied field; the third term is the Zeeman interaction. The rhombic term $E(\hat{S}_x^2 - \hat{S}_y^2)$, which vanishes in axial symmetry, represents the major origin of the mixing of states on either side of the energy barrier on which depends the occurrence of QTM. In effect, the larger is E, the larger is the tunneling matrix element mixing two states, and the larger are the resulting tunnel splitting Δ and the tunneling probability,

P. The latter also depends inversely on the field sweep rate, as expected from standard Landau−Zener theory.[29] Of course, the *E* term makes QTM feasible, but it is still necessary to have transverse fields before QTM can actually occur, and even in the absence of external applied fields, these are provided by the transverse components of dipolar and exchange fields from neighboring molecules and hyperfine fields from ^{55}Mn ($I = 5/2$) nuclei. Note that the presence of transverse fields is essential for QTM in half-integer spins, where parity effects are operative and crystal-field terms alone cannot cause tunneling to occur.[30]

The observed hysteresis loops in Figure 9 can now be rationalized. The lowering of the symmetry of these Mn$_4$ complexes from the virtual C_{3V} of the majority of the family to the only virtual C_S of **9**−**12** will lead to a significant increase in the rhombic anisotropy parameter, *E*, and in the resulting tunneling rates. As a result, a very large QTM step is seen at zero field, even at the lowest temperatures (and fastest sweep rates) when tunneling occurs only by the $M_S = \pm 9/2$ channel for which the tunnel rates should be the slowest. The large step at zero field and the fast tunneling rates that it indicates also rationalize the ac data showing a faster relaxation rate for the lower-symmetry complexes **9**−**12** compared with the virtual C_{3V} symmetry Mn$_4$ complexes, even though the former have the larger *D* value. In effect, although the larger *D* values of **9**−**12** lead to a larger barrier *U*, their faster QTM rates resulting from their larger *E* values short-cut this barrier and lead to a net smaller effective barrier (U_{eff}) for **9**−**12**. This explanation qualitatively rationalizes all the ac and hysteresis data on the basis of the low symmetry and the resulting increased *E* value, but it was felt essential to obtain independent and quantitative support for it, and for this we turned to high-frequency electron paramagnetic resonance spectroscopy, a technique capable of providing a reliable indication of the magnitude of the rhombic anisotropy.

Single-Crystal, High-Frequency Cavity-Based EPR Spectroscopy of 9 and 10. High-frequency electron paramagnetic resonance (HFEPR) spectroscopy is a powerful technique for the magnetic characterization of molecular species with large anisotropy. Absorption peaks observed in HFEPR spectra result from transitions between sublevels of the ground and low-energy spin states. At low temperatures, only a few of these sublevels are populated and, therefore, only a few peaks should be seen in the EPR spectrum. As the temperature is increased, more states become populated, and more peaks are observed. The analysis of spectra for different high-spin complexes can provide extremely precise information such as the exact value of the ground-state spin,[31] the magnitude and sign of *D*,[32] the location

in energy of excited spin states relative to the ground state[33] and, most importantly, information concerning transverse spin Hamiltonian parameters that are responsible for the magnetic quantum tunneling, e.g. the rhombic *E*-term.[34,35] However, the $(2S+1)$-fold energy level structure associated with a large molecular spin *S* necessitates EPR spectroscopies spanning a wide frequency range.[36,37] Furthermore, large zero-field splittings due to the significant crystalline anisotropy and large S_T values demand the use of frequencies and magnetic fields considerably higher (40 GHz to several 100 GHz, and up to 10 T) than those typically used by the majority of EPR spectroscopists.[36,37,38]

All [Mn$_4$O$_3$X]$^{6+}$ complexes studied to date (X = Cl$^-$, Br$^-$, F$^-$, and $^-$O$_2$CMe)[39] possess virtual C_{3v} symmetry, which provides these molecules with a dominant uniaxial magneto-crystalline anisotropy. However, in the solid state, the [Mn$_4$O$_3$(O$_2$-CPh-R)]$^{6+}$ complexes **9**−**12** have only virtual C_S symmetry, and HFEPR measurements were carried out to complement the magnetic studies. The complete Hamiltonian (*H*) that describes these compounds is shown in eq 9.

$$H = D\hat{S}_z^{\,2} + E(\hat{S}_x^{\,2} - \hat{S}_y^{\,2}) + \mu_0\, g\, \mu_B\, \hat{S} \cdot H + B_4 \hat{O}_4 + H' \quad (9)$$

This is the same equation as eq 8, except that it also includes the operator $\hat{O}_4$, which characterizes fourth order crystal-field interactions (e.g., the axial $B_4{}^0\hat{O}_4{}^0$ term), and *H′*, which includes all other effects such as weak intermolecular couplings and/or electron−nuclear hyperfine interactions;[40] the other symbols have the meanings defined earlier. The second term parametrizes the rhombic distortion of the crystal field, i.e., the dominant transverse term due to the crystal field, and represents the main focus of these HFEPR studies; *E* ($< |D/3|$) parametrizes the strength of this interaction, and $\hat{S}_x$ and $\hat{S}_y$ are the *x*- and *y*-axis spin projection operators. Within the appropriate zero-field $\hat{S}_z$ basis, $\hat{S}_x$ and $\hat{S}_y$ do not commute with $\hat{S}_z$. Consequently, as mentioned earlier, the rhombic term in eq 9 represents a major source of mixing of states on opposite sides of the energy barrier to magnetization reversal, thereby making possible the QTM. However, as again mentioned already, transverse fields play a crucial role in driving QTM in these half-integer spin systems, as originally pointed out by Wernsdorfer et al.[30] The most likely source of such fields (contained within *H′*) are intermolecular dipolar or exchange interactions, and nuclear spins.

We have investigated the *D* and *E* crystal field parameters of **9**−**12** using both powder-average and single-crystal HFEPR techniques. Numerous recent studies of high-symmetry SMMs,

(27) (a) Tsai, H.-L.; Hendrickson, D. N.; Eppley, J. J.; de Vries, N.; Folting, K.; Christou, G. *J. Chem. Soc., Chem. Commun.* **1994**, 1745. (b) Eppley, H. J.; Tsai, H.-L.; de Vries, N.; Folting, K.; Christou, G.; Hendrickson, D. N. *J. Am. Chem. Soc.* **1995**, *117*, 301. (c) Aubin, S. M. J.; Sun, Z.; Guzei, I. A.; Rheingold, A. L.; Christou, G.; Hendrickson, D. N. *J. Chem. Soc., Chem. Commun.* **1997**, 2239. (d) Kuroda-Sowa, T.; Nakno, M.; Christou, G.; Hendrickson, D. N. *Polyhedron* **2001**, *20*, 1537. (e) Soler, M.; Wernsdorfer, W.; Abboud, K. A.; Huffman, J. C.; Davidson, E. R.; Hendrickson, D. N.; Christou, G. *J. Am. Chem. Soc.* **2003**, *125*, 3576.
(28) Caneschi, A.; Ohm, T.; Paulsen, C.; Rovai, D.; Sangregorio, C.; Sessoli, R. *J. Magn. Magn. Mater.* **1998**, *177*, 1330.
(29) Olson, R. E. *Phys. Rev. A* **1970**, *2*, 121.
(30) Wernsdorfer, W.; Bhaduri, S.; Boskovic, C.; Christou, G.; Hendrickson, D. N. *Phys. Rev. B* **2003**, *65*, 180403.
(31) Edwards, R. S.; Maccagnano, S.; Yang, E.-C.; Hill, S.; Wernsdorfer, W.; Hendrickson, D. N.; Christou, G. *J. Appl. Phys.* **2003**, *93*, 7807.
(32) Rumberger, E.; Hill, S.; Edwards, R. S.; Wernsdorfer, W.; Zakharov, L. N.; Rheingold, A. L.; Christou, G.; Hendrickson, D. N. *Polyhedron* **2003**, *22*, 1865.
(33) Zipse, D.; North, J. M.; Dalal, N. S.; Hill, S.; Edwards, R. S. *Phys. Rev. B* **2003**, *68*, 184408.
(34) Hill, S.; Edwards, R. S.; Jones, S. I.; North, J. M.; Dalal, N. S. *Phys. Rev. Lett.* **2003**, *90*, 217204.
(35) Hill, S.; Takahashi, S.; Edwards, R. S.; North, J. M.; Dalal, N. S. http://xxx.lanl.gov/abs/cond-mat/0401515 (Jan. 27, 2004).
(36) Hill, S.; Perenboom, A. J.; Dalal, N. S.; Hathaway, T.; Stalcup, T.; Brooks, J. S. *Phys. Rev. Lett.* **1998**, *80*, 2453.
(37) Hill, S.; Edwards, R. S.; Jones, S. I.; Maccagnano, S.; North, J. M.; Aliaga, N.; Yang, E.-C.; Dalal, N. S.; Christou, G.; Hendrickson, D. N. *Mater. Res. Soc. Symp. Proc.* **2003**, *746*, 253 (Materials Research Society).
(38) (a) Hill, S.; Dalal, N. S.; Brooks, J. S. *Appl. Magn. Reson.* **1999**, 16, 237. (b) Mola, M.; Hill, S.; Goy, P.; Gross, M. *Rev. Sci. Inst.* **2000**, *71*, 186.
(39) (a) Aubin, S. M. J.; Wemple, M. W.; Adams, D. M.; Tsai, H.-L.; Christou, G.; Hendrickson, D. N. *J. Am. Chem. Soc.* **1996**, *118*, 7746. (b) Li, Q.; Vincent, J. B.; Libby, E.; Chang, H. R.; Huffman, J. C.; Boyd, P. D. W.; Christou, G.; Hendrickson, D. N. *Angew. Chem.* **1988**, *100*, 1799.
(40) (a) Park, K.; Novotny, M. A.; Dalal, N. S.; Hill, S.; Rikvold, P. A. *Phys. Rev. B* **2002**, *65*, 14426. (b) Park, K.; Novotny, M. A.; Dalal, N. S.; Hill, S.; Rikvold, P. A. *Phys. Rev. B* **2002**, *66*, 144409. (c) Hill, S.; Maccagnano, S.; Park, K.; Achey, R. M.; North, J. M.; Dalal, N. S. *Phys. Rev. B* **2002**, *65*, 224410.
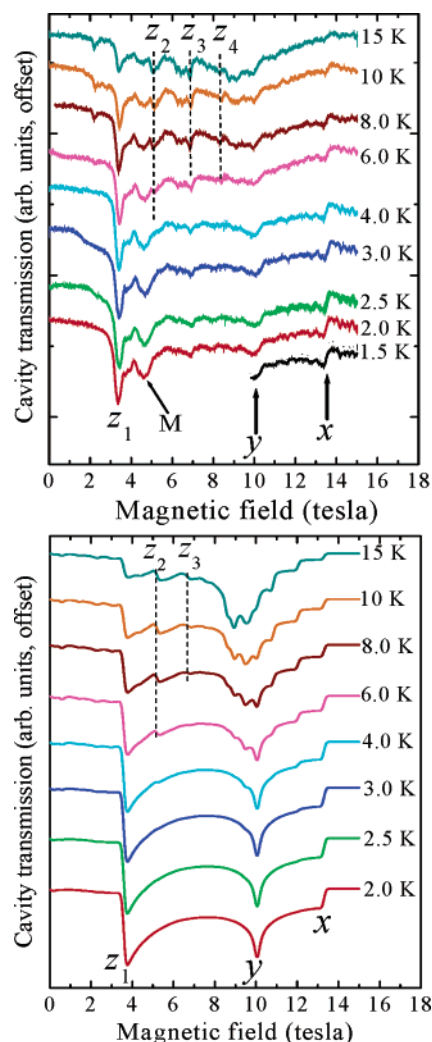
Figure 10. Experimental data (top) and simulations (bottom) of the microwave transmission through the cavity containing a powder sample of [Mn₄O₃(O₂CPh-Me)₄(dbm)₃] (**10**) at the indicated temperatures vs applied magnetic field strength; the frequency was 249 GHz. See the text for an explanation of the labeling of the resonances.

including several Mn_4 systems,[5,41] have demonstrated the power of single-crystal HFEPR capabilities. However, in the case of the present complexes, such an approach is greatly complicated due to the intrinsically low-symmetry of the structure, and the resulting difficulties in locating the principal magnetic axes of a single-crystal. In principle, this could be achieved using a goniometer, but this is incompatible with the HFEPR technique which, at present, allows only for sample rotation in a single plane.[34,35,38] For this reason, the simplest way to obtain the D and E parameters is to perform measurements on a fine powder of randomly oriented microcrystals. Thus, most of the data presented below were obtained, as described in the Experimental Section, on a microcrystalline powder sample of [Mn₄O₃(O₂-CPh-*p*-Me)₄(dbm)₃] (**10**) in a solid pellet of eicosane wax. We also carried out single-crystal studies on [Mn₄O₃(O₂CPh)₄-(dbm)₃] (**9**), but we cannot evaluate the E term using this method.

Figure 10 (top) depicts several experimental plots of the microwave transmission through the cavity containing a powder sample of **10**, as a function of the applied magnetic field strength; the frequency was 249 GHz and the various temperatures are indicated in the figure. The spectra reveal several

sharp features labeled x, y, z_i, or M. These correspond to resonant absorptions of microwaves due to the EPR response of crystallites that are oriented such that the applied field is along one of their principal magnetic axes—either x, y, or z. The sharpest feature is labeled z_1. Since this resonance persists to the lowest temperatures investigated, we infer that it corresponds to an excitation from the ground state of the $S = {}^9\!/_2$ multiplet. The same is true for resonances x, y and M. The three peaks x, y and z_1 may be explained very well using the Hamiltonian of eq 9 with the following parameters: $D = -0.646$ cm^{-1}, $E = 0.140$ cm^{-1}, $B_4^0 = -3.5 \times 10^{-5}$ cm^{-1}, $g_z = 1.85$ and $g_z = g_y = 2.00$ (see below). To illustrate this agreement, we have simulated the powder spectra in Figure 10 (top) using the software program SIM,[42] assuming a completely random distribution of orientations of the crystallites; these simulations are shown in Figure 10 (bottom). Again, three singular features are apparent at the lowest temperatures, which occur at exactly the same fields as the resonances labeled x, y, and z_1 in Figure 10 (top). As noted above, these resonances are related to the x, y, and z axes spectra of the individual crystallites.

While the positions of the sharp features in the experimental data and the simulations are in agreement, the overall shapes of the curves differ slightly. We suspect that this is due to field alignment of a significant number of the crystallites in the eicosane pellet, which was fairly loosely packed. Such an alignment of a fraction of the crystallites can lead to a significant enhancement of the easy (z-) axis components of the spectrum relative to the hard (xy) plane response. Consequently, the z resonances become stronger, sharper and more symmetric relative to the x and y components. The field alignment results from the significant torque on the $S = {}^9\!/_2$ SMMs at low temperatures, in combination with the negative magnetocrystalline anisotropy (D). Indeed, this method is often used to align polycrystalline samples in order to mimic single crystal measurements. However, the alignment is only affective along one axis, and the orientations remain random within the plane transverse to the applied field. Thus, although the reorientation of some fraction of the sample influences the shapes of the HFEPR spectra, this does not influence the locations of the features in the spectra. Therefore, one may reliably estimate crystal-field parameters from data such as those in Figure 10.

Further comparisons in Figure 10 between the experimental data and the simulations reveal additional resonances as the temperature is increased. These features correspond to transitions from excited states within the $S = {}^9\!/_2$ ground-state spin manifold. We have labeled some of the peaks (z_2, z_3, z_4) corresponding to the easy (z-) axis components of the spectra, since these are clearly visible in the experimental plots (presumably due to the field alignment effect discussed above). However, the x and y components of the excited state spectra are not clearly discernible in the data. In addition to the resonances labeled x, y, and z_1, a relatively strong peak M is seen just above z_1, which persists to the lowest temperatures investigated. Its position just to the high field side of the z_1 resonance suggests an excitation of similar origin, perhaps resulting from a minority Mn_4 species with an approximately 10−20% smaller D-value. While great

(41) Edwards, R. S.; Hill, S.; Bhaduri, S.; Aliaga-Alcade, N.; Bolin, E.; Maccagnano, S.; Christou, G.; Hendrickson, D. N. *Polyhedron* **2003**, *22*, 1911.
(42) Jacobsen, C. J. H.; Pedersen, E.; Villadsen, J.; Weihe, H. *Inorg. Chem.* **1993**, *32*, 1216.
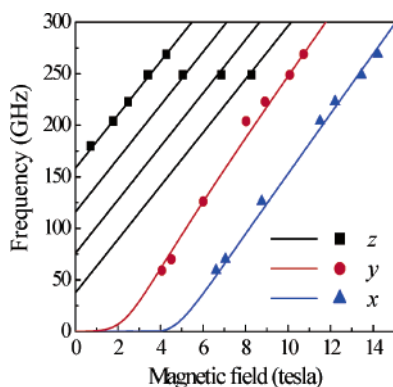
Figure 11. Plot of the experimental field positions of the x, y, and z_i resonances (solid points) as a function of frequency (z_2, z_3, and z_4 are only available from the 249 GHz measurements, which were taken at higher temperatures). The solid lines are the fits of the data, from which the Hamiltonian parameters given in the text were obtained.
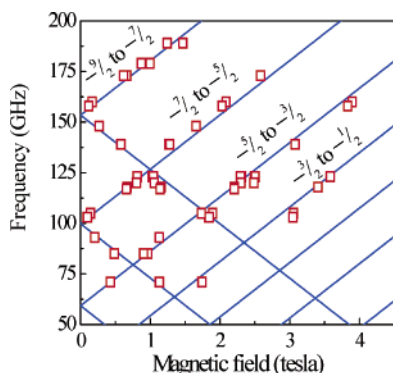
Figure 12. Plot of the experimental field positions of resonances obtained at 15 K for a single-crystal of [Mn$_4$O$_3$(O$_2$CPh)$_4$(dbm)$_3$] (**9**). Superimposed are fits to the data (solid lines), from which the D and B_4^0 parameters given in the text were obtained.

care was taken to avoid solvent loss during the preparation of the powder sample, it is known that these complexes are rather air sensitive, which could result a significant fraction of molecules having a different compliment of solvent molecules. Despite this unexplained aspect of the spectra, the main features of the EPR spectra are extremely robust, and are in good agreement with simulation.

As a final constraint on the Hamiltonian parameters for [Mn$_4$O$_3$(O$_2$CPh-p-Me)$_4$(dbm)$_3$], we repeated the low temperature (2 K) measurements at many different frequencies from 49 to 269 GHz. In Figure 11, we plot the locations of the x, y, and z_i resonances as a function of frequency (z_2, z_3, and z_4 are only available from the 249 GHz measurements which were taken at higher temperatures). Superimposed on the data are fits to the data points from which the Hamiltonian parameters quoted above were obtained. From the spacings of the z_i resonances, one can deduce the value of the fourth order parameter B_4^0. It is also clear from this plot which peaks correspond to the easy (z-) axis and hard (xy-) responses of the sample, i.e., the z_i resonances have positive zero-field offsets, while the x and y resonances have negative zero-field offsets. These assignments, together with the temperature-dependent data in Figure 10, enable us to verify that the sign of D is negative, as expected for a SMM. Of course, this was already confirmed from hysteresis measurements.

Finally, in Figure 12, we plot the positions of resonances obtained at 15 K for a single-crystal of [Mn$_4$O$_3$(O$_2$CPh)$_4$(dbm)$_3$]

(**9**). As mentioned above, the single crystal measurements are complicated due to the problem of locating the high-symmetry directions of the crystal. Furthermore, the unit cell contains pairs of molecules with their z-axes tilted relative to each other, i.e., there are two easy magnetization directions for this crystal. Nevertheless, by extrapolating the positions of resonances to zero magnetic field, one may accurately obtain the zero-field level splittings, and thus the D and B_4^0 Hamiltonian parameters. The scatter in the data is likely due to sample misalignment. However, the zero-field extrapolations, obtained by superimposing fits to eq 9 on to the data, are extremely reliable. These extrapolations yield the following crystal field parameters: $D = -0.567$ cm^{-1} and $B_4^0 = -1.73 \times 10^{-4}$ cm^{-1}. We speculate that the smaller D value obtained for this complex may be related to the reduced distortion of the cube, resulting in a smaller projection of the single-ion anisotropy onto the z-axis for the molecule.

Conclusions

The controlled potential electrolysis of [Mn$_4$O$_2$(O$_2$CPh-R)$_7$-(dbm)$_2$]$^-$ complexes has proved to be a useful method for the synthesis of the corresponding [Mn$_4$O$_3$(O$_2$CPh-R)$_4$(dbm)$_3$] complexes. The procedure is facilitated by the insolubility of the products in the electrolysis solvent, providing a ready means to their isolation in pure form, uncontaminated by the supporting electrolyte. Although the preparations are relatively small scale, they are nevertheless a convenient means of accessing these complexes, whose synthesis is not available by an alternative route. A crystal structure has confirmed the identity of complex **10**, and its low symmetry as a result of the η^2-binding mode of the unique, central carboxylate ligand, with consequently only virtual C_S symmetry for these complexes. ^{1}H NMR spectral studies in CD$_2$Cl$_2$ have established that the complexes retain their structural integrity in this solvent, but that they exhibit effective C_{3V} symmetry in solution, which we have assigned to rapid (on the ^{1}H NMR time scale) rotation of the central carboxylate group.

Detailed magnetic susceptibility studies have established that the lower symmetry has little effect on the pairwise exchange parameters in these molecules, and as a result the ground state of complexes **9**−**12** is $S = 9/2$, the same as the higher symmetry complexes. However, the D value is significantly greater, and we can qualitatively correlate this with the greater projection of the Mn^{III} single-ion anisotropies onto the molecular anisotropy axis as a result of the η^2-binding mode of the unique, central carboxylate ligand and the consequent opening up of one face of the Mn$_4$ distorted-cubane structure. As a result of their $S = 9/2$ ground state and the significant D value, complexes **9**−**12** have a significant barrier to magnetization relaxation and thus function as single-molecule magnets (SMMs). However, they exhibit fast QTM in zero field, as reflected in a very large QTM step at zero field in the hysteresis loops. In fact, this fast QTM has precluded detailed magnetization vs time decays studies to obtain relaxation kinetic data that would allow an Arrhenius plot to be constructed from which could be determined the effective barrier to magnetization relaxation, U_{eff}. Nevertheless, it is clear from the combined dc and ac data that the magnetization relaxation rates for these low-symmetry complexes are greater than for the higher symmetry Mn$_4$ complexes, even

though their *D* values are higher. This apparent paradox is assigned to the greater transverse anisotropy parameter *E* resulting from the lower symmetry, and consequently the greater QTM rates in **9**−**12** that short-cut what would otherwise be the larger barriers to relaxation. In fact, this provides an important take-home message from this work, namely that in trying to increase the relaxation barriers so that SMMs that function at higher temperatures may be obtained, it is important to not just increase *S* and/or *D*, but to also keep *E* as small as possible to minimize the QTM rates through the barrier.

In any event, complexes **9**−**12** described in this work are unusual, low symmetry versions of the Mn$_4$ SMMs and represent important new additions that continue to provide invaluable insights on the influence of symmetry on the magnetic properties of molecular nanomagnets, information that will be crucial as this still relatively young field continues to be developed.

Supporting Information Available: X-ray crystallographic files in CIF format for complex **10**. 2CH$_2$Cl$_2$, ^{1}H NMR spectra, and magnetism fits. This material is available free of charge via the Internet at http://pubs.acs.org.

JA047527M